

Emerging two-dimensional tellurides

Saif Siddique ^{1,†}, Chinmayee Chowde Gowda ^{2,†}, Solomon Demiss ^{1,3,†}, Raphael Tromer ⁴, Sourav Paul ⁵, Kishor Kumar Sadasivuni ⁶, Emmanuel Femi Olu ³, Amreesh Chandra ⁷, Vidya Kochat ⁵, Douglas S. Galvão ⁴, Partha Kumbhakar ^{1,*}, Rohan Mishra ^{8,*}, Pulickel M. Ajayan ^{9,*}, Chandra Sekhar Tiwary ^{1,2,*}

Two-dimensional (2D) materials are at the forefront of current materials research due to their exciting and unique properties. 2D tellurides are emerging materials which are yet to be fully explored. To provide an overview of this emergent field, in this review, we discuss the structure, properties, synthesis methods, and applications of selected 2D tellurides, with stoichiometry of $M_x Te_y$, and $M_x N_y Te_z$, (M, N are metal atoms). We present a summary of the latest advances in modeling, experimental synthesis, and characterization of 2D tellurides. Additionally, stress and strain-induced tunability of the physical properties have been reviewed, with a focus on the application of 2D tellurides in electronic, optoelectronic, and magnetic devices. We have discussed many emergent quantum properties of these materials. Finally, we conclude with a perspective on the future of 2D metal tellurides.

Keywords: 2D tellurides; Topological properties; Weyl semimetals; Superconductivity; Charge density waves; Thermoelectric property; Strain-tunability

Introduction

Two-dimensional (2D) materials have currently become the focus of research with applications in several fields such as opto-electronics, spintronics, sensors, thermoelectrics, photoelectrics, superconductors, energy storage, and topological insulators. Chalcogenides are the materials containing one or more chalco-

gens: sulfur (S), selenium (Se), and tellurium (Te). A great deal of research has been aimed towards the synthesis and study of 2D metal chalcogenides owing to their interesting physicochemical properties, and applications like optoelectronics, semiconductor devices [1–3], energy storage, battery electrodes [4,5], superconductivity, electrocatalysis [6–9], thermoelectricity and gas sensing. In their review, Popescu et al. [10] have summarized the development of chalcogenides over time. The field of 2D materials that started with the isolation of graphene layers in 2004 has grown to include many more materials such as transition-metal dichalcogenides (TMDCs), most popularly MoS₂, layered double

¹ Metallurgical and Materials Engineering, Indian Institute of Technology Kharagpur, West Bengal 721302, India

² School of Nano Science and Technology, Indian Institute of Technology Kharagpur, West Bengal 721302, India

³ Materials Science and Engineering, Jimma Institute of Technology, Jimma University, Jimma, Ethiopia

⁴ Applied Physics Department, University of Campinas, Brazil

⁵ Materials Science Centre, Indian Institute of Technology Kharagpur, West Bengal, 721302, India

⁶ Center for Advanced Materials, Qatar University, Qatar

⁷ Department of Physics, Indian Institute of Technology Kharagpur, West Bengal, 721302, India

⁸ Department of Mechanical Engineering & Materials Science, and Institute of Materials Science & Engineering, Washington University, St. Louis, MO 63130, USA

⁹ Department of Materials Science and NanoEngineering, Rice University, 6100 S Main Street, Houston, TX 77005, USA

^{*} Corresponding authors.

E-mail addresses: Kumbhakar, P. (parthakumbhakar2@gmail.com), Mishra, R. (rmishra@wustl.edu), Ajayan, P.M. (ajayan@rice.edu), Sekhar Tiwary, C. (chandra.tiwary@metal. iitkgp.ac.in).

[†] Equal contribution

hydroxides, metal oxides, metal nitrides/carbides (MXenes), transition metal halides, hexagonal boron nitride (hBN), black phosphorous (BP) and other elemental 2D materials such as phosphorene and arsenene [11,12]. Many of the 2D materials, especially the TMDCs, MXenes, and BP have intrinsic bandgaps; and when their dimensionality is reduced, the band structure as well as excitonic emissions becomes favorable for optoelectronic devices [13,14]. BP has a unique in-plane anisotropic structure, whereas graphene and other TMDCs have in-plane centrosymmetry. The larger ionic radius and the broadening of dbands of tellurium as compared to sulfur and selenium, result in relatively small bandgap ($E_g \le 1.2 \text{ eV}$) providing device applications operable in the infrared wavelength range. In terms of optoelectronic applications, graphene was amongst the first few materials which attracted much attention due to its wide bandwidth operation, faster carrier dynamics, and no need for optimization through bandgap engineering or chirality control; hence finding various applications in the field of nonlinear optics [15]. The TMDCs have the tendency to behave as metallic, semiconducting or insulating at times. Covalent bonds between the transition-metal and chalcogen atoms along with the weak interlayer van der Waal (vdW) forces make it easy to exfoliate these chalcogenides into lower-dimensional structures. Several properties of 2D materials depend on their thickness (number of layers). 2D Te, unlike TMDCs, have a helical-chain structure with strong chemical bonds within the layer. This results in the preferable growth of 1D Te morphology, imparting the interesting properties, as we will see. Furthermore, the trilayer structure of Te provides tellurene a higher stability and superior properties than other 2D materials.

2D Tellurides are the emerging materials in the so called "postgraphene age". With high carrier mobility, larger surface area and IR spectral absorption, these materials show a lot of promise. Tellurium has a high atomic number (Z = 52) and exhibits large spin-orbit coupling (SOC), due to which the properties displayed by metal tellurides differ from their sulfide and selenide counterparts. As mentioned above, the larger ionic radius and broader d-bands in tellurides results in smaller bandgaps when compared to sulfides and selenides. For instance, 1H MoS₂ has a bandgap energy of E_g = 1.89 eV, while 1H MoTe₂ has a smaller bandgap ($E_g = 1.23 \text{ eV}$). The 2H condensed state is a trigonal prismatic structure of transition-metal tellurides (TMTs) with twolayer Te atoms having mirror symmetry along the metal atom layer; whereas in 1T and 1T' condensed states, there is an octahedral sandwich structure [16]. Fascinating structural transitions are observed in 2D tellurides which are responsible for variation in electrical, optical and other physical properties [17]. Thermoelectricity is one domain where tellurides outperform other materials. It has been challenging for the researchers to develop materials that show a good thermoelectric figure of merit (ZT), the term quantifying the efficiency of such materials. The best ZT values of ~ 1 are exhibited by tellurides like Bi₂Te₃, BiAsTe, and PbTe [18]. The heavier Te atom (as compared to S and Se) limits lattice vibrations, reducing the thermal conductivity. The diverse crystal structures and exciting properties such as high magnetization, large SOC, and structural phase transitions have contributed to the increased interest in tellurides [19-21]. These materials also display a variety of properties that can be chemi-

cally and/or mechanically tuned. Many of the 2D tellurides, especially the ternary tellurides, show a transition from an indirect to direct bandgap as the number of layers are reduced. The indirect-to-direct bandgap transition plays a crucial role in increasing the light absorption and luminescence efficiency that is observed in photodetectors, solar cells, and light-emitting diodes (LEDs). Magnetism is a challenging property to achieve in 2D materials. According to the Mermin-Wagner theorem [22], long-range ferromagnetic ordering is prohibited in the 2D isotropic Heisenberg model. However, after the successful synthesis of CrGeTe₃ [23], an intrinsic ferromagnetic material, the domain of magnetic 2D materials with applications in spintronic-related devices opened up, as other 2D materials exhibiting magnetism like VX₂ (X = Se, Te), Fe₃GeTe₂, and FeTe, along with some non-tellurides like CrI₃, MnSe₂, and FePS₃ were synthesized [24-28]. Table S1 compares the properties of different 2D mateirals [29-60] and aims at providing a perspective on where 2D tellurides stand amongst other 2D materials (see Supporting Information).

Many of the tellurides also show emergent quantum properties such as superconductivity and charge density waves (CDW). In very low temperatures, changes in pressure and magnetic field can induce phase changes called quantum phase transitions (QPT). Superconductivity is a result of QPT. In the quantum world, many states of matter exist by virtue of spontaneous symmetry breaking as per the Landau-Ginzburg-Wilson framework [61,62]. Superconductivity is explained by breaking the gauge symmetry [63]. Below a critical temperature, called the superconductive transition temperature (T_c) , the electrical resistance becomes zero in superconductors, and current flows without any loss of energy. Tellurides such as PdTe₂. ZrTe₃, $GdTe_3$ perform extremely well as superconductors, with T_c of about 2 K. A majority of superconductors have T_c in the range of 1 K to 10 K. The Fe-Te systems, however, show very high $T_{\rm c}$ (as high as 70 K). Some 2D materials also undergo Peierls transition (distortion of periodic lattice in a 1D crystal breaking its perfect ordering) to show CDW instability. Along with the lattice distortion, static modulation of conduction electrons lowers the total energy of the solid. CDW and energy band variations are observed in lower-dimensional Te systems. While the spontaneous symmetry breaking in the Landau-Ginzburg-Wilson theory explains many of the quantum states, including superconductivity, crystallinity, and magnetism, it fails to work for some of the newly discovered quantum electronic phases, notably, topological states. These states came into focus after topological insulators (TIs) were discovered, that conduct electric current only along the edges of a 2D material and are insulating in the bulk. The spontaneous symmetry breaking theory cannot distinguish between TIs and the topologically trivial insulators. In TIs, SOC and time-reversal symmetry combine to form the state of matter [64]. Other topological materials have been subsequently discovered with applications in spin electronic devices and quantum information technology [64-67]. Tellurides also host many of these novel topological states: Bi₂Te₃ and ZrTe₅ are excellent 2D topological insulators [68,69]. Materials having semimetallic electronic structures also exhibit nontrivial band topology. The existence and lack of Fermi surface define traditional metals and insulators, respectively; however, topological

semimetals have bands crossing (touching) at the Fermi energy [70]. In topological semimetals, fermions (a type of subatomic particles) arise as low-energy excitations. The semimetals host two types of fermions – Dirac and Weyl [71]. The Dirac fermions are protected by different crystal symmetries. And when timereversal or inversion symmetry is broken, a spin degenerate fermion splits into two Weyl fermions, changing the closed Fermi surface to open Fermi arcs. Weyl semimetals have a linear crossing of two bands at the Fermi level. They have multiple Fermi arcs, which originate from topologically protected surface-states [72]. Thus, these materials show novel quantum phenomena of chiral anomaly-induced, negative magnetoresistance (MR), and supersymmetry. A Weyl semimetal (Type-I) has linearlydispersed non-degenerate bands that cross each other at the Weyl points (Fig. 1(a)). For Dirac semimetals, the Fermi level has four linearly crossing bands and has a double-degenerate Dirac cone (Fig. 1(c)). Both the Weyl and Dirac semimetals obey something called the Lorentz invariance, T(k) < U(k), where T(k)and U(k) are the linear kinetic and potential terms describing the Hamiltonian for the two fermions: H(k) = T(k) + U(k) [70,73]. If the Lorentz invariance is violated, then the Dirac and Weyl cones tilt by a significant amount, as can be seen in Fig. 1(b, d). These are termed as the type-II Dirac/Weyl fermions. PtTe $_2$ is a type-II Dirac semimetal [73]. The type-II Weyl fermions were first predicted in the orthorhombic T $_d$ phase of WTe $_2$ [71,74]. The T $_d$ phase of MoTe $_2$ has been also established as a type-II Weyl semimetal [75,76].

Recently, intensive theoretical and experimental works with exciting results have ensured increased interest in 2D tellurides, which indicates upcoming years of research in the field. There are extensive reviews consolidating the studies on the "beyond graphene materials", and vdW layered structures [11,77–79]. A recent review [17] highlights the structure and electronic properties of selected layered transition metal tellurides with an emphasis on their synthesis and electronic devices. In this work, we compile and consolidate the information on an exhaustive set of 2D tellurides. The review aims at providing an overview of the crystal structure, synthesis methods, properties, and applications of these materials. We summarize several binary tellurides as well as discuss the intriguing properties that develop by the addition of a third element (Fig. 2). We look into the diversity of properties in these 2D layered materials, including the optical,

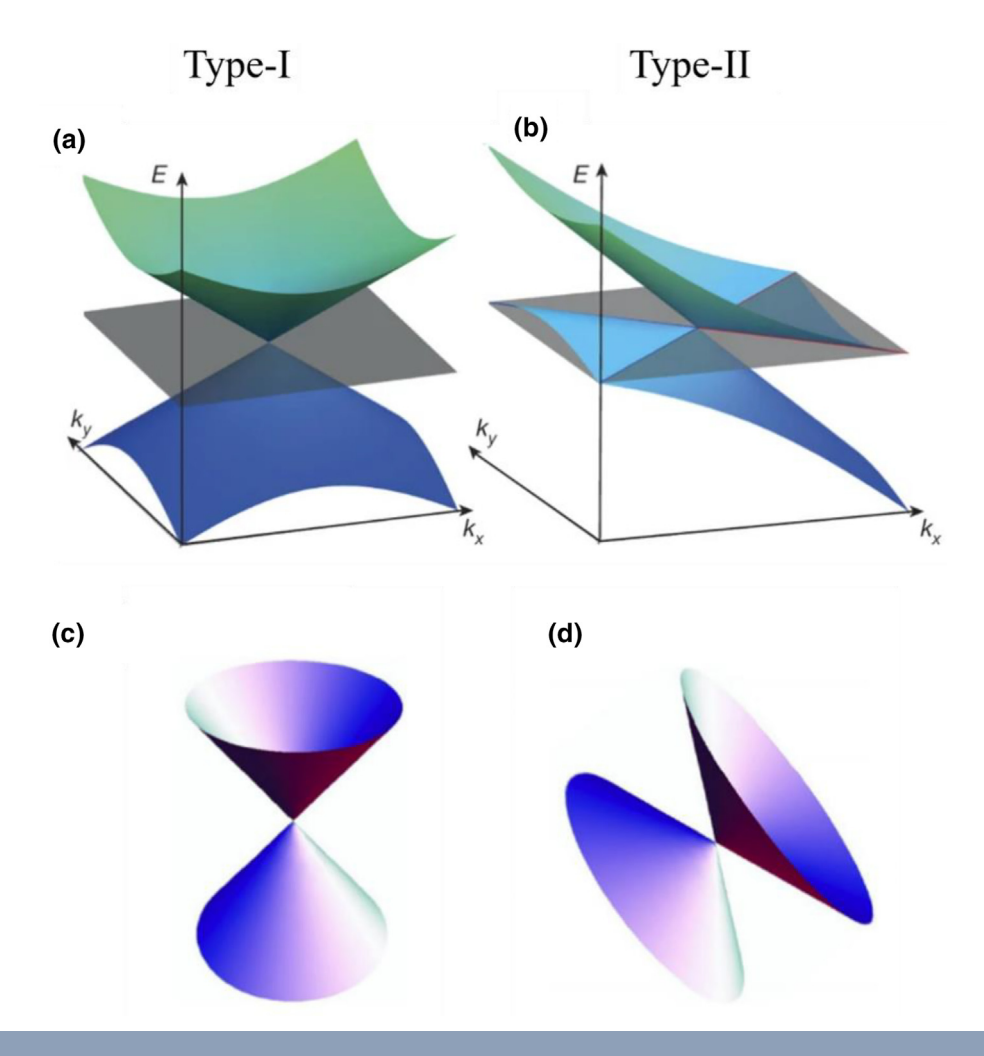
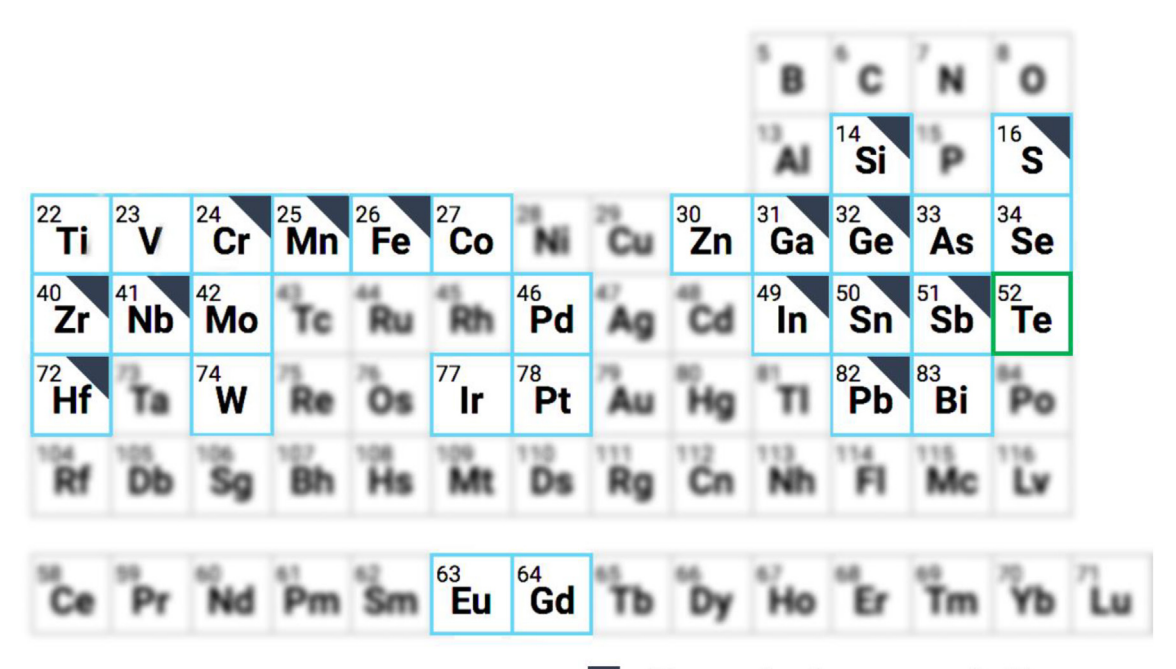


FIGURE 1

The two types of Weyl semimetals are shown with a non-degenerate Dirac cone. The type-I Weyl semimetal (a) has a point like Fermi surface. (b) The type-II phase appears as the contact point between e^- and h^+ pockets. The grey plane represents the Fermi level [71]. (c) Schematic of type-I Dirac fermion (d) Strongly titled Dirac cone at the topologically protected touching point between the e^- and h^+ pockets (type-II Dirac fermions) [73].



Elements that form ternary tellurides

FIGURE 2

Periodic Table showing the metals (in blue) and Tellurium (in green) that form the binary tellurides discussed in this review.

electronic, photo-electrochemical, magnetic, and quantum properties. We then conclude by providing prospects for research in this field, along with challenges that need to be addressed to unlock the potential of 2D tellurides in vast areas of applications.

Synthesis methods

Synthesis strategies for 2D materials can be classified into two broad groups: top-down and bottom-up approaches. The topdown approach is mostly used for layered materials and involves cleaving of atomically thin layers from bulk crystals. It can also be extended for materials with a higher c/a ratio. Mechanical forces and acoustic vibrations are the two most commonly employed techniques to cleave layers of materials. While the top-down method offers an inexpensive and facile route to obtain 2D layers, a precise control over the number and size of layers is not possible. The bottom-up approach addresses this by synthesizing 2D materials directly from the scratch, giving control over the morphology and size of 2D sheets. Fig. 3 lists some of the common synthesis methods that are used to synthesize 2D materials in general. Many of the metal tellurides have a layered structure with stacks of tellurium-metal-tellurium (Te-M-Te) units bound by vdW forces. Top-down approaches like mechanical and chemical exfoliation have become the favorite synthesis routes for the 2D materials having weak vdW forces. Methods like vapor phase transport, molecular beam epitaxy, chemical vapor deposition, pulsed laser deposition (PLD), and other solution-based methods are bottom-up methods and are suitable for producing 2D structures on a large scale. For more details on synthesis methods of 2D materials, readers are requested to go through these excellent reviews [17,80]. In the supplementary information, we briefly discuss the important parameters of the commonly used synthesis methods for 2D

materials. Table 1 summarizes the synthesis methods employed to obtain some of the 2D tellurides discussed in this review [81–93]. Supporting Information.

A lot of tellurides discussed in the review are yet to be synthesized. Density Functional Theory (DFT) calculations have been used to study their formation and cohesive energies, dynamic stabilities, and possible synthesis methods. As seen from Table 1, CrPbTe₃, SnSb₂Te₄, Ge₂STe, Sn₂STe, and HfGeTe₄ have only been predicted to exist. A negative value of the cohesive energy indicates thermodynamic stability of the material. For example, CrPbTe₃ has a cohesive energy of -3.44 eV, similar to that of 2D silicon. From its phonon dispersion, dynamic stability is also expected [94]. These results suggest that the material will be stable once synthesized. The cleavage energy can also indicate the success of mechanical/liquid-phase exfoliation. For instance, monoclinic bulk As₂Te₃ has a cleavage energy of 0.36 J m⁻² (like graphene). They can, thus, be exfoliated to get 2D sheets (which has already been achieved using CVD) [95]. Similarly, the cleavage energies of CrGeTe₃ and CrSiTe₃ are also comparable to that of graphite [96]. PdTe2 is a material that exists in two phases pentagonal and hexagonal. But only its hexagonal phase has been synthesized experimentally, even though it has been shown that p-type penta-PdTe2 is a better thermoelectric material, with a ZT value higher than the well-known Bi-Te thermoelectrics [97,98]. DFT calculations were employed and the pentagonal phase was found to have dynamic stability. It was predicted that its monolayers could be fabricated using CVD [97]. All these materials show exceptional properties, as we see later, and are capable of bringing significant advancement in materials science research. One of the aims of this review is to bring forward such opportunities by better understanding the current research in this field.

TABLE 1
Synthesis methods, applications, and crystal structure of some tellurides.

Synthesis methods	2D tellurides	Applications	Crystal Structure and space group	Ref.
Chemical Vapor Transport, Co- evaporating Knudsen Effusion Cell, Epitaxial Growth	TiTe ₂	Optoelectronics, Electronic Devices	<i>P</i> 3 <i>m</i> 1	[99–103]
Pulsed laser deposition, Co-evaporation	ZrTe ₂	Quantum and Electronic Devices		[104,105]
Atmospheric pressure CVD, Molecular Beam Epitaxy, Exfoliation	VTe ₂	Electrocatalysts for Hydrogen Evolution Reaction		[106,107]
Co-evaporating from Knudsen Cells & Theoretical predictions	PdTe ₂	Thermoelectric, Superconductors	Ti Te	[97,98]
Chemical Vapor Deposition, Hydrothermal Method	CoTe ₂	Electrochemical Applications, Electrocatalysts	P3m1 and Pnnm	[108–110]
Chemical Vapor Transport, CVD, MBE, PVD	MoTe₂,	Weyl semimetal	Co Te	[111–115]
	$Mo_xW_{1-x}Te_2$	Optoelectronic Memory Devices Electronic Beam Collimation		J.
Plasma-enhanced CVD, Theoretical Predictions	As₂Te₃	Lens Thermoelectric Devices	Mo Te	[95,96,116]
Mechanical Exfoliation, Self-flux method	FeTe, Fe _{1+y} Te	Magnetic Devices, Superconductors	P4/nmm	[26,117–119]
Mechanical Exfoliation, MBE	Fe ₃ GeTe ₂	Magnetoresistance, Storage	Fe	[120–126]
		Devices, Low-power spintronics	مزمزه	
			b	
			Fe Ge Te	

TABLE 1 (CONTINUED)

Mechanical Exfoliation, Theoretical Predictions Criptes Spintronic Devices Criptes Ferromagnetic, Spintronic Devices Photovolicitis, Ferromagnetic, Ferromagnetic, Fer	Synthesis methods	2D tellurides	Applications	Crystal Structure and space group	Ref.
Theoretical Predictions SnSb ₂ Te ₄ Mechanical Exfoliation, Theoretical Predictions Mechanical Predictions Mechanical Predictions Theoretical Predictions GaGeTe Theoretical Predictions Theoretical Predictions GaSeTe Theoretical Predictions Chemical Vapor Transport, Theoretical Predictions Chemical Prediction		CrGeTe₃	Spintronic Devices	b a Cr. To	[23,96,129,130]
Mechanical Exfoliation, Theoretical Predictions GaGeTe Photovoltaics, FETs, Quantum Devices, Data Storage Devices Theoretical Predictions Ge2STe Optoelectronic Devices Theoretical Predictions Sn2STe Optoelectronic Devices Theoretical Predictions Theoretical Predic	Theoretical Predictions	CrPbTe₃		P4/nbm	[94,131]
Mechanical Exfoliation, Theoretical Predictions GaGeTe Photovoltaics, FETs, Quantum Devices Devices Ga Ge Te Theoretical Predictions Theoretic	Theoretical Predictions	SnSb ₂ Te ₄	Light-Harvesting Devices,		[132]
Theoretical Predictions Theoretical Predictions Theoretical Predictions Theoretical Predictions Theoretical Predictions Theoretical Predictions Chemical Vapor Transport, Theoretical Predictions Theoretical Predictions Theoretical Predictions Chemical Vapor Transport, Theoretical Predictions Theoretical Predictions InTeF HfGeTe₄ ZrGeTe₄ Electronic Devices Electronic Devices Cmc2₁ [137] Cmc2₁ [138] [140] Zr Ge Te		GaGeTe	Photovoltaics, FETs, Quantum	Ga Ge Te	[133–136]
Theoretical Predictions Theoretical Predictions Theoretical Predictions Theoretical Predictions Theoretical Predictions Theoretical Predictions Chemical Vapor Transport, Theoretical Predictions Theoretical Predictions Theoretical Predictions Theoretical Predictions InTeF HfGeTe₄ ZrGeTe₄ Electronic Devices Electronic Devices FETs, Optoelectronic Devices Cmc2₁ [138] [139] [140] Zr Ge Te₄ Te	Theoretical Predictions	Ge₂STe	Optoelectronic Devices	_	[137]
Theoretical Predictions Chemical Vapor Transport, Theoretical Predictions HfGeTe ₄ ZrGeTe ₄ Electronic Devices Electronic Devices Cmc2 ₁ [139] Cmc2 ₁ [140]	Theoretical Predictions	Sn ₂ STe	Optoelectronic Devices	_	[137]
	Theoretical Predictions Chemical Vapor Transport, Theoretical	HfGeTe₄	Electronic Devices	c a b	[139]
Self-flux Method, Theoretical Predictions Nb ₂ SITe ₄ Optoelectronic Devices P2 ₁ /c [141,142]	Calf flow Marks at The constitut Day that we	NII- CIT-	Outs distance in Decision		[1.41.1.42]
Nb Si Te	seii-iiux Method, Theoretical Predictions	ND ₂ 511e ₄	Optoelectronic Devices		[141,142]

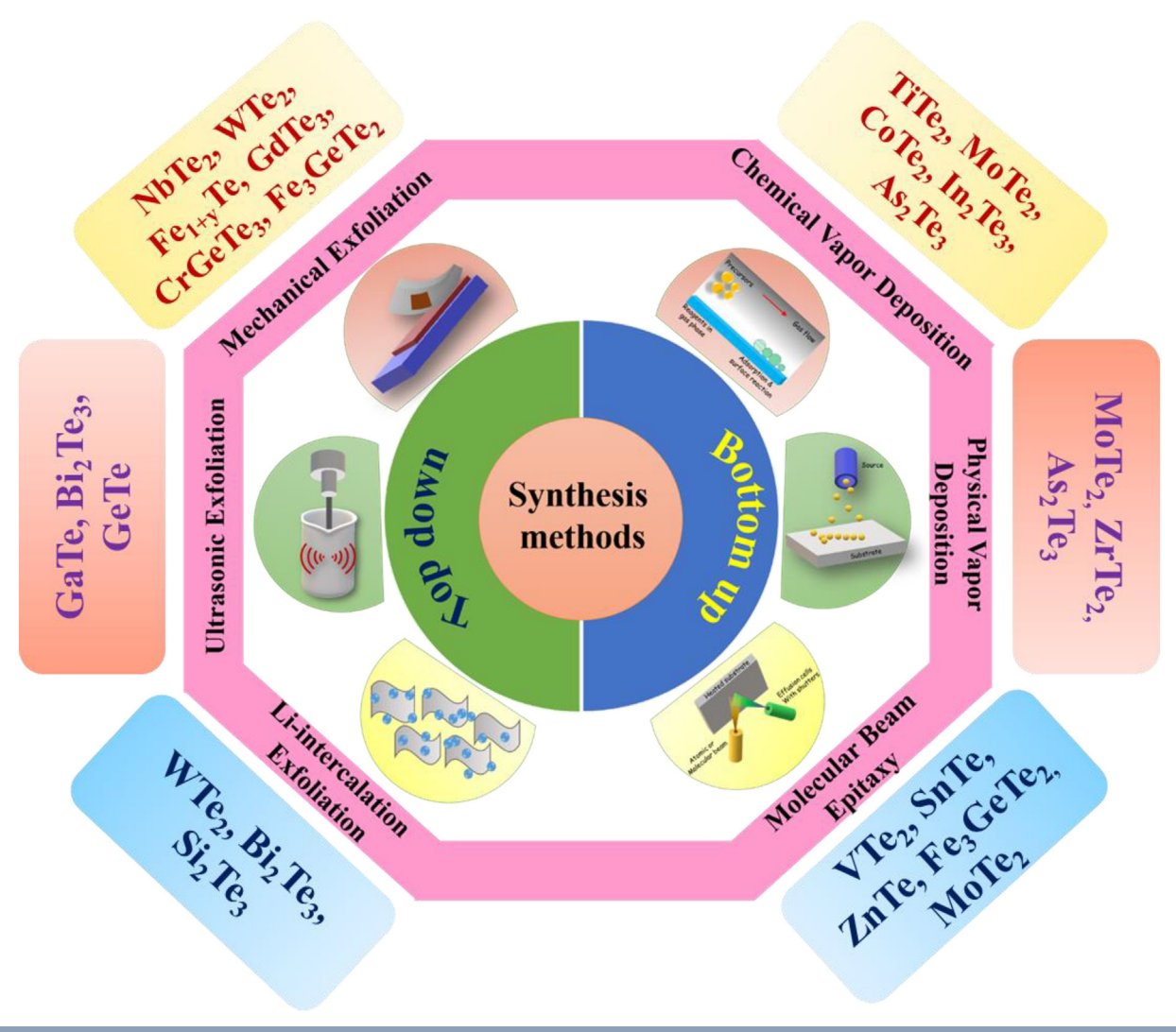


FIGURE 3

Schematic of some of the common synthesis techniques of 2D materials. The figure also lists a few tellurides prepared using the methods.

Crystal structure

In this section, the crystal structures of some of the 2D tellurides of the form $M_x \text{Te}_v$ and $M_x N_v \text{Te}_z$ are discussed. The elemental Te monolayers, tellurenes are stable in 1T-MoS₂-like (α-Te) phase, while metastable tetragonal (β -Te) and 2H-MoS₂-like (γ -Te) phases and have been explored for their enhanced structural properties. The trigonal structure of bulk Te consists of helical chains along the [001] direction, which indicates that the zdirection pointing along the c-axis qualitatively differs from the layering structures of tellurene [143]. The atomic structure of trigonal Te is strongly anisotropic, making its nanomaterials grow into anisotropic structures - nanowires, nanotubes, and nanorolls. Due to this anisotropy, TeSe2 was developed as an alternative to tetragonal Te [144]. Another compound close to elemental Te is SeTe. Its monolayer has two types of atomic structure: a planar structure where SeTe has a center of symmetry, and a buckled structure having mirror symmetry along the 45° diagonal of the a- and b-axis of the lattice (Fig. 4(d)) [69].

The TMTs of the type MTe_2 typically crystallizes with a layer of M atoms sandwiched between two Te atomic layers forming Te-

M-Te trilayers. The trilayers are found to be in two structural phases – 2H and 1T. The 2H phase has a trigonal prismatic coordination of the metal atoms, while 1T has an octahedral one. The '2' and '1' in the notation stands for the number of layers in the unit cell [145]. In most cases, the 2H phase has higher stability and shows superior properties than 1T [146]. Tellurides such as TiTe₂, ZrTe₂, VTe₂, PtTe₂, NbTe₂ and MoTe₂ all have this structure (Fig. 4(a)) [99,111,147,148]. TiTe₂ is an anisotropic system, and therefore, even in its 2D state, it retains its 3D nature to some degree; for example, the electronic structure is similar to that of bulk material [100]. IrTe₂ also has a trigonal phase at room temperature (RT). But as the temperature is decreased, it transitions into a lot of other phases including some topological ones [149].

Among the TMTs, the cobalt system is an interesting material due to its magnetic, electrochemical, and catalytic properties. $CoTe_2$ exhibits two different phases – orthorhombic marcasite and a trigonal CdI_2 -type structure [108,109]. It exists in non-stoichiometric, tellurium-deficient compositions to maintain stability. Similar to cobalt-based tellurides, zinc telluride (ZnTe) is also a semiconductor that has been studied for its thermoelectric

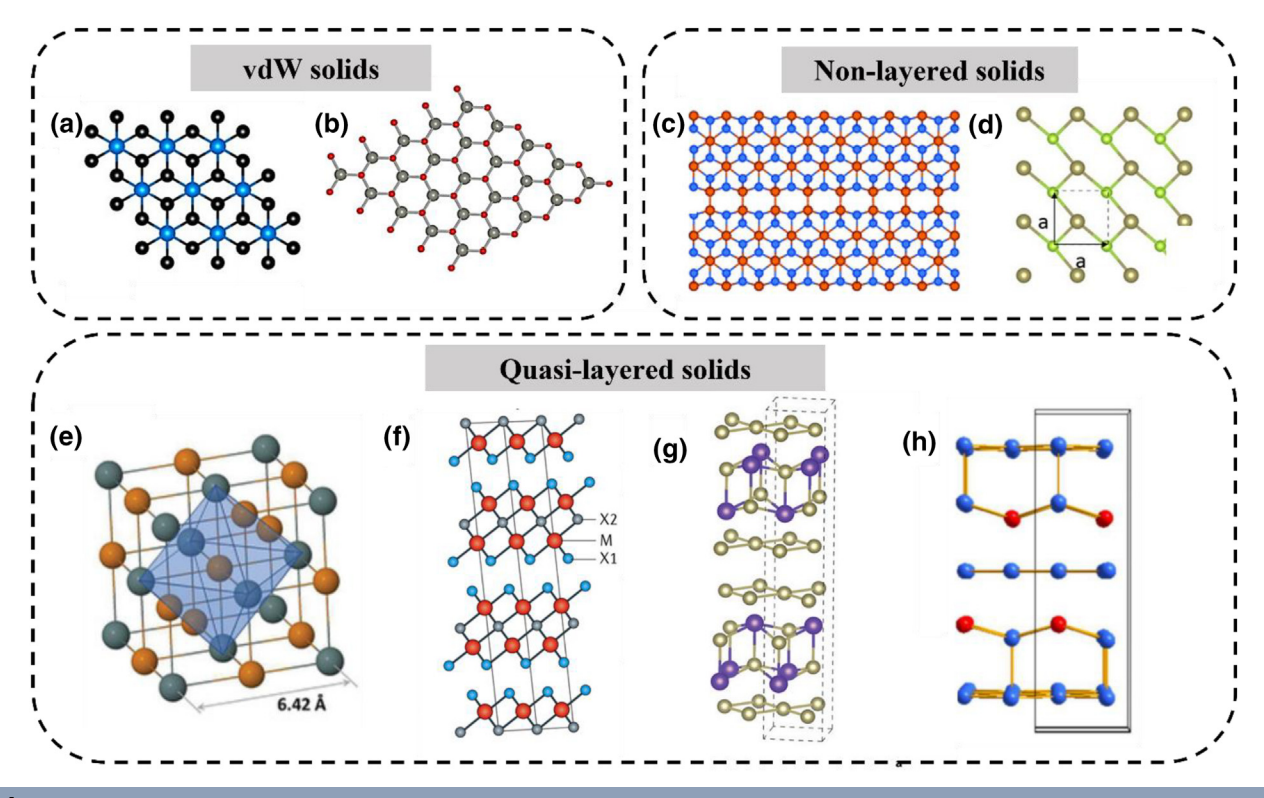


FIGURE 4

(a) The top and side view of the TiTe₂, ZrTe₂, and 1T-VTe₂ (Te-M-Te trilayer) crystal structure [101,104,106], (b) Top view of hexagonal ZnX (X = O, S, Se, Te) [183], (c) Top view of monoclinic GaTe (Blue circles – Ga atoms, Red circles – Te atoms) [152] (d) Top view of the square structures of the b-SeTe monolayer (Green – Se atoms, Brown – Te atoms) [160], (e) The rock-salt structure of β -SnTe (Orange – Te atoms) [158], (f) The rhombohedral tetradymite structure of group V tellurides (X1 and X2 are the Te sites) [159] (g) Crystal structure of GdTe₃ [161], (h) Crystal structure of EuTe₄ with square atomic Te sheets and alternating Eu-Te slabs (Blue – Te atoms) [162].

and optoelectronic applications. Its heterostructures with other materials, such as MoS_2 and In_2Te_3 , have also been reported to have superior catalytic properties [150,151]. Given the versatility of ZnTe polycrystals, the same can be expected for 2D ZnTe layers. Monolayer ZnTe is predicted to have a hexagonal structure with a lattice parameter of 4.40 Å and exhibiting a germanenelike structure (Fig. 4(b)). An sp^3 hybridization exists between the Zn-Te 2D layers.

The group III tellurides also demonstrate a rich variety of crystal structures. The Gallium Telluride (Ga-Te) system is one of the important members of the III-VI compounds. GaTe and Ga₂Te₃ have low formation energy which facilitates easier exfoliation of the bulk samples into 2D sheets, even though neither have a layered structure. In GaTe, two Ga atoms are sandwiched between two Te atoms, forming a Te-Ga-Ga-Te structure (Fig. 4 (c)) [21,152]. Ga₂Te₃ has a zinc blende structure with the Ga atoms forming an intermediate layer between the Te atomic layers (Fig. 4(b)). The hexagonal Te lattice shrinks to form an fcc structure [153]. Both of them show vacancy planes, which results in ultralow lattice thermal conductivity required for highperformance thermoelectric materials [154]. Similar to GaTe, InTe too consists of four sublayers stacked in the sequence Te-In-In-Te. However, unlike its gallium counterpart, In₂Te₃ exists in two crystalline phases – anti-fluorite (α) and zinc-blende (β) structures. β-In₂Te₃ only exists at higher temperatures while the α - phase is stable at lower temperatures, with a transition temperature of 600 [155].

The tellurides of group IV and V are best known for their thermoelectric properties. Tin Telluride (SnTe) is one of them. It has Sn deficiency, because of extra Te atoms creating two holes in the valence band, making it a p-type material. In the ambient conditions, it has a NaCl-type cubic structure (Fig. 4(e)) that transforms to orthorhombic under pressure, which can be then exfoliated. There is another structural transformation to rhombohedral at the Curie temperature, where SnTe forms a ferromagnetic state [156–158]. The group V elements, such as As, Bi, and Sb combine with Te to form rhombohedral structures. They are excellent thermoelectric materials and topological insulators. Because of their similarity to Bi₂Te₂S structure these materials are called tetradymites. In general, tetradymites are M2X3 compounds (where M is a group V element; X is a chalcogen), but other mixtures of M and with two different types of X (e.g., Bi₂Te₂Se) are also included in the group (ternary tetradymites). Since both M and X have similar electronegativities, anti-site defects are formed which is the reason behind their exceptional thermoelectric performance. The tetradymite structure has a rhombohedral symmetry with layers of X1-M-X2-M-X1 stacked along the c-axis (Fig. 4(f)). X1 and X2 are distinct sites, and this allows the formation of ternary tetradymites [159]. Because of the nature of bonds, the X2 bond is more ionic, and hence, more electronegative chalcogen occupies it. It is very difficult to obtain stoichiometric Bi₂Te₃ using normal synthesis methods because of the ease of formation of defects. Arsenic telluride (As₂Te₃) exists in two forms: monoclinic α -phase, which can be transformed into a rhombohedral β -phase under pressure. Both of these phases show excellent absorbance in the range of 1.6 to 3.2 eV. As already mentioned, its rhombohedral phase performs well for thermoelectric applications [116].

Rare earth tellurides form something called quasi-layered compounds: they are not vdW solids but respond to exfoliation methods. For example, single crystals of GdTe₃ (Fig. 4(g)) [161] and EuTe₄ [162], obtained by the self-flux method, can be exfoliated to obtain 2D sheets. All the quasi-2D polytellurides (RTe_n; n = 2, 2.5, 3) share a common structure of consecutive square Te sheets separated by corrugated R-Te slabs. The crystal structure of EuTe₄ (Fig. 4(h)) shows that there is a regular, nearly square net made of a monolayer of Te atoms. Because of the square Te sheets, the compound has susceptibility towards Peierls instabilities.

Like other 2D systems, many of the ternary tellurides exhibit layered hexagonal structures. Fe₃GeTe₂, SnSb₂Te₄ and GaGeTe, all have a hexagonal structure in their 2D forms [120,132,133]. Owing to their layered structure, the three materials have been synthesized by exfoliation methods. In addition to the scotchtape method that gives 4.8 nm thick sheets of Fe₃GeTe₂ [163], its 2D films of 0.82 nm thickness were also synthesized using MBE on (111) GaAs [120]. The CrXTe₃ (X = Si, Ge, and Pb) system has also been extensively investigated. CrSiTe₃ and CrPbTe₃ have a hexagonal crystal structure and their monolayers (ML) can be obtained by exfoliation [94,127]. Bulk CrGeTe₃, however, crystallizes into a rhombohedral crystal structure belonging to the R3 space group [130]. It also has a layered structure with a large interlayer vdW gap ($d_0 = 3.3 \text{ Å}$) making it possible to obtain 2D flakes from single crystals using mechanical exfoliation [96]. Adding fluorine (F) in the InTe monolayers results in InTeF having a buckling-honeycomb structure with space group P3m1. This honeycomb monolayer forms a tetrahedral structure, where each In atom bonds with three Te atoms and one F atom.

An orthorhombic structure is also commonly found in 2D ternary tellurides. 2D Ge₂STe and Sn₂STe monolayers have a puckered structure in the space group Pmn2₁. Both of these materials have not been synthesized and their atomic structures, electronic structures, optical properties, and thermodynamic stabilities have been reported using DFT calculations [137]. HfGeTe₄ and ZrGeTe₄ also exhibit orthorhombic crystal structure but they belong to Cmc2₁ space group [139]. These group IV 2D metal germanium chalcogenides, MGeX (M = Hf, Zr; X = S, Se, Te) have chalcogen poor phases and exist in PbFCl structure, i.e., the Ge and X atoms form a negative anion [140]. Although ultrathin ZrGeTe4 flakes of 28 nm have been obtained using the scotch-tape method [164], 2D HGT is yet to be synthesized [140]. Bulk Nb₂SiTe₄ is a layered material that is formed by sandwiching (Nb, Si) between two Te atoms. Few-layer Nb₂SiTe₄ has also been synthesized using the scotch-tape method and has an orthorhombic crystal structure [148].

Physical properties and emerging applications

Tellurium has eight stable isotopes, with an atomic weight of 127.60 \pm 0.03 for its most stable isotope. ¹³⁰Te (33.8%) and ¹²⁸Te (31.7%) are the most abundant isotopes, and ¹²⁵Te and ¹²³Te with I=1/2 can be used in NMR. However, the only crys-

talline form of tellurium that shows electrical conductivity exists as a spiral chain polymer. It has a smaller electronegativity than oxygen and show decreased ionicity and increased bond covalency. The structural confinement in 2D tellurides enhance their physiochemical properties such as superconductivity, thermoelectricity, and the existence of topological phases. The 2D structure also exposes larger surface-active sites for possible binding of molecules/ions or charge conduction making them suitable for electrochemical applications. Like other chalcogenides, in tellurides too, by applying strain and varying the number of layers, properties can be tuned as per requirement. Recent developments in theoretical and experimental techniques have led to a lot of exciting properties in the 2D tellurides.

Electronic and transport properties

2D tellurides show a diverse range of electronic properties, as evident from their band structure (metallic, semiconducting, and insulating) as well as the existence of quantum phases like CDW and topological states. The transition metal tellurides (TMTs) are best known for their electronic properties. They include MoTe₂ that may exist in three different structural phases: 2H, 1T', and T_d. In its 2H phase, MoTe₂ is a semiconductor, a Weyl semimetal in its 1T' phase. Its T_d phase shows topological Fermi arcs. These arcs are found at the boundary between the $e^$ and h^+ pockets and are enlarged to a significant amount. The 2H monolayer has a direct bandgap of 1.1 eV. Experiments show that this direct bandgap in monolayer and bilayer changes to an indirect one in its tetralayer. The trilayer exhibits both nearly identical direct and indirect gaps [112]. The presence of a nearzero density of states and a very low resistivity near the Fermi energy leads to the formation of a pseudogap as a result of the few electronic states, thus, making the material a semimetal. Materials like ZrTe₂ (Fig. 5(a)) and NbTe₂ also show semimetallic state as revealed by the DFT calculations [104,105,165]. Hall Effect measurements of NbTe2 give a carrier concentration of $n = 5.46 \times 10^{21} \text{ cm}^{-3} \text{ having mobility, } \mu = 6.9 \text{ cm}^{2} \text{ V}^{-1} \text{ s}^{-1},$ and resistivity, $\rho = 1.74 \times 10^{-4} \,\Omega$ cm [165]. It also has a large pseudo-gap around the Fermi surface. The quasi-2D layered semimetal shows anisotropic magneto-transport properties. An anomalous linear MR of max 30% at 9 T was observed showing the coexistence of a large quasi-2D Fermi surface and a small Fermi pocket [166].

The presence of heavy Te atoms with a large SOC results in a larger splitting of the valence band in MoTe₂ compared to MoS₂ and MoSe₂. Moreover, MoTe₂ has a vertical stacking with a noncentrosymmetric space group Pmn21 and due to lack of inversion symmetry, Weyl Fermions exist [112]. It shows strong anisotropic band dispersions where Fermi crossings of both electron and hole type are observed along Γ -Y direction, but only holelike Fermi crossings are observed along the Γ -X direction. One interesting property of MoTe₂ is the ease of control over doping and its reversibility. Electrothermal doping (electrothermal annealing by applying an electric field under vacuum conditions) allows us to control the type of doping (p- or n-type) in 2H-MoTe₂ transistors [167]. Under ambient conditions, O₂ and H₂O molecules adsorb on the surface of the material. Applying electric field heats up the conducting channels in MoTe₂ causing adsorbates with less adsorption energy to leave the surface.

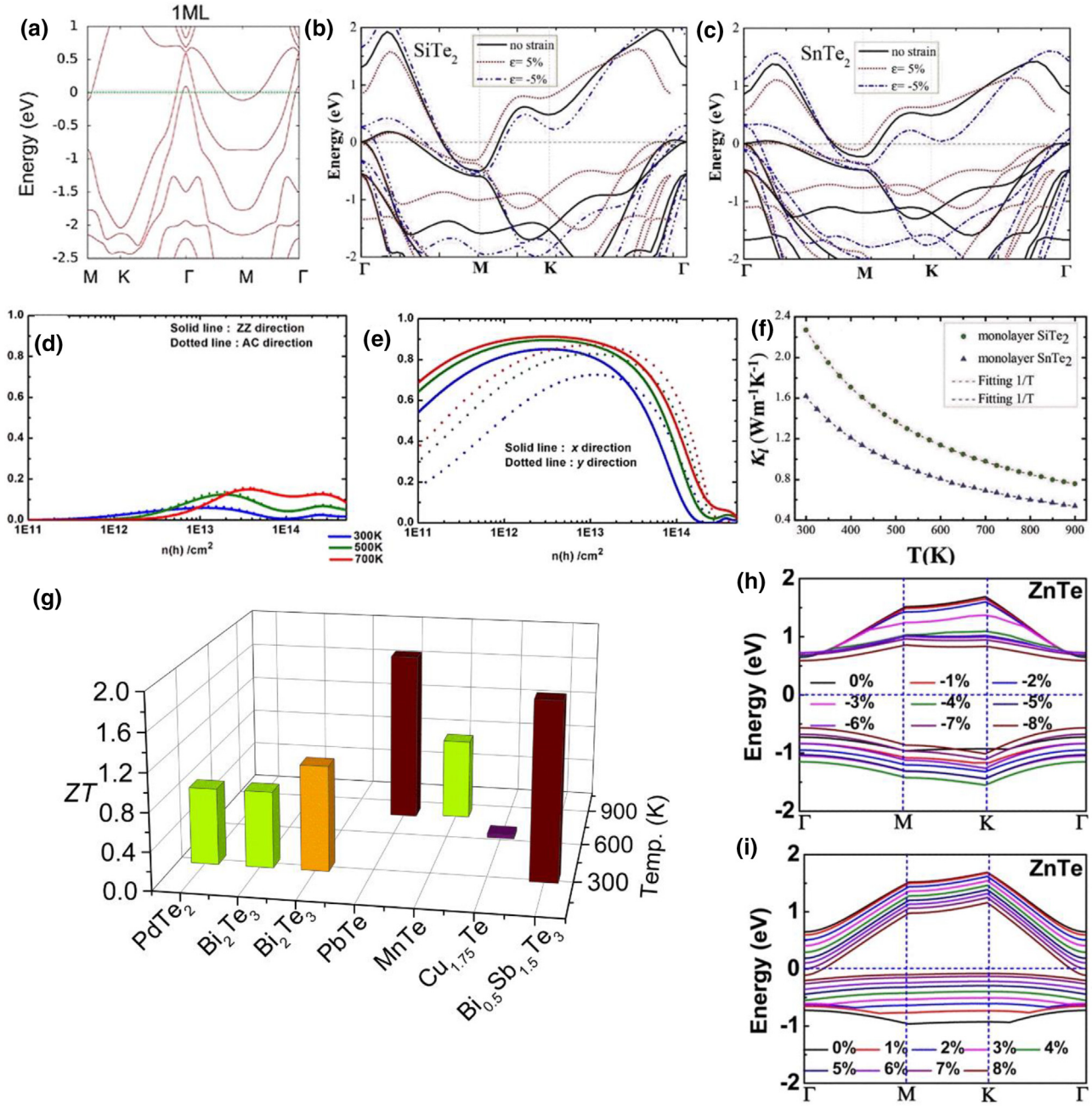


FIGURE 5

(a) The calculated band structure of 1ML ZrTe₂ showing the semimetallic nature [105], (b) Calculated band structure of SiTe₂ and (c) SnTe₂ [146], (d) Calculated ZT figures of merit plotted as a function of carrier concentration of p-type hexa-PdTe₂, and (e) p-type of penta-PdTe₂ [98], (f) Temperature dependent lattice thermal conductivity of a monolayer SiTe₂ and SnTe₂ from 300 to 900 K [146], (g) A comparison of the ZT values of some tellurides [98,172,173,175,177,184,185], (h) Near band edge of ZnTe under compressive stress and (i) tensile stress [183].

Excess electrons are left behind: hence n-type doping. When this material is re-exposed to air, physisorptions of O_2 and H_2O results in a p-type doping. Since no external dopant or gas is required, the process is extremely simple and offers a precise control over the doping. Thus, the field-effect transistors (FETs) manufactured out of $MoTe_2$ has considerable potential for adaptive logic circuits.

It has been experimentally demonstrated that the distorted 1T $MoTe_2$ monolayer shows room temperature ferroelectricity [113]. In most of the materials, there are lower limits to the number of

layers below which the ferroelectric behavior disappears. Also, the $T_{\rm c}$ for ferroelectricity decreases as the number of layers decreases. Ferroelectricity in MoTe₂ monolayers make it a promising material for logical and memory devices. Layer-dependent electronic properties are also observed in PtTe₂. It changes from a semiconductor to a type-II Dirac semimetal with a strongly tilted Dirac cone along the Γ -A direction [73]. The presence of defects further changes the bandgap of PtTe₂ monolayers. This presents a possibility of changing the properties of the material through defect engineering [168]. PtTe₂ can also

form a heterojunction with Si and can be used as a photodetector because of its broadband sensitivity in the wavelength range of $200{\text -}1650$ nm. The heterojunction so formed is of high stability [169]. 2D PtTe2 is also an excellent electrothermal material, capable of converting electrical to thermal energy with high efficiency. This property is useful in thermochromic displays, heaters, defrosters, thermotherapy, and heating textiles [170,171].

2D tellurides also show exceptional thermoelectric properties. Improving the thermoelectric performance involves an optimization between contraindicative properties: high electrical conductivity but low thermal conductivity for a high ZT [172]. Nanostructuring restricts the scattering of phonons, which lowers the lattice thermal conductivity ($\kappa_{\rm I}$), while maintaining high electrical conductivity, thus enhancing ZT. A bottom-up wetchemical synthesis method has been used to realize 2D Bi₂Te₃. ZT values were two-to-four times higher than bulk Bi₂Te₃ [173,174]. PbTe₃ is widely known for its band degeneracy and "dopability" which increases its ZT value [175]. DFT studies predict that the ZT value of PdTe2 is higher than Bi2Te3 [97]. The electrical conductivity over relaxation times for tellurides is more than sulfides and selenides, resulting in superior thermoelectric performance. Marfoua and Hong [98] theoretically investigated the thermoelectric properties of both p-types and n-types of Hexa and Penta-PdTe2 and found that the best performance was given by p-type Penta-PdTe2 (Fig. 5(d, e)). Thermoelectric properties are also predicted in the monolayer 1T phase of SiTe₂ and SnTe₂ [146]. Their monolayers have ultralow κ_L resulting in ZT of 0.46 at 600 K and 0.71 at 900 K for SiTe₂ and SnTe₂ ML, respectively. SnTe2 has a strong anharmonicity resulting in a lower κ_L of 1.62 W m⁻¹ K⁻¹ as compared to 2.27 W m⁻¹ K⁻¹ for SiTe2 (Fig. 5(f)). Composite structures of Bi0.5Sb1.5Te3 (BST) nanosheet films, obtained by spin coating followed by drop casting, show ZT as high as 1.0 [176]. $Cu_{1.75}$ Te nanosheets also show enhanced thermoelectric behaviour than bulk structures [177]. Excellent thermoelectric properties are also observed in devices fabricated using ternary Nb₃SiTe₆, with thermoelectric power of \sim 230 µV K⁻¹ at 370 K where the electrical resistivity was below 1.5 m Ω cm [178]. Fig. 5(g) shows a comparison plot of thermoelectric figure of merit of some of the 2D tellurides.

Unlike TMTs, the group III-tellurides are mostly semiconductors. 2D GaTe has an indirect bandgap of 1.65 eV [21], while the bandgap of InTe is wider with a value of 2.37 eV. These bandgap values are thickness-dependent and can also be engineered by stress or chemisorption [58]. Exposure to air can decrease the bandgap of 2D GaTe to 0.8 eV. Similar effect of the oxygen functionalization on 2D InTe has also been investigated. It narrows the bandgap to 0.21 eV decreasing the effective carrier masses and increasing the work function [179]. The 2D InTe sheet with oxygen functionalization becomes inert towards oxidation and degradation. Therefore, it is an ideal material to produce the quantum spin Hall effect at RT, allowing the development of high-speed and dissipation-free transport devices. The bandgap of 2D InTe also makes it a promising material for water photocatalysis due to a bandgap higher in value than 1.23 eV (water splitting value) as well as the favorable positions of the band edges [180]. Its wide-bandgap is also suitable for applications in light-emitting devices and photodetectors. InTe is softer than MoS_2 and thus can be easily strained, making it a good candidate for strain band engineering.

Chang et al. [156] studied SnTe and showed the formation of domain structures, band bending and lattice distortions, and also demonstrated ferroelectricity in its thin films. *Ab-initio* investigations on the interaction between 2D SnTe and different substrates reveal that it is possible to tune the ferroelectricity of 2D SnTe films in contact with Ni, Pd, Pt, Si, Ge, CaO, and MgO substrates [157]. Both SiTe₂ and SnTe₂ monolayers have a semimetallic character which arises as the conduction band minimum (CBM) overlaps with the valence band maximum (VBM) (Fig. 5(b, c)) and retain this semimetal property even under biaxial strain [146]. This, however, is different for As₂Te₃. The band structure of α -As₂Te₃ changes by applying pressure [95]. The indirect bandgap closes at above 6 GPa, with a semiconductor-tometal transition. Its electronic properties are anisotropic, with the carrier mobility of holes is higher than that of electrons.

The $M\beta\alpha$ phase of TeSe₂ is similar to orthorhombic Te and was the first one to be studied theoretically amongst the TeSe₂ phases. It has a wide indirect bandgap of 2.39 eV that converts into a direct bandgap under a tensile strain, making it suitable for mechanical sensors and piezoelectric devices [181]. This $M\beta\alpha$ phase lacks inversion symmetry giving rise to spontaneous polarization, having value similar to SnTe, another 2D ferroelectric material that has been fabricated. The change in polarization, caused by small stresses and/or electric fields, is an important factor when considering the application of the material in ferroelectric devices [144]. The HyT (hexagonal) phase of TeSe₂ monolayer has an indirect bandgap of 0.94 eV as calculated using the HSE06 exchange–correlation [182]. The bandgap increases with the application of compressive strain and decreases with tensile one.

Strain engineering can also provide stability to materials. The ZnTe monolayer has a buckling band structure, as shown in Fig. 5(h, i), with a direct bandgap of 1.37 eV. There is a dynamic instability in ZnTe, due to the presence of imaginary (negative) frequencies in the phonon dispersion [183]. A small strain shifts these into the real domain, thus increasing the stability. Application of a tensile strain of 2% provides dynamic stability to the monolayer and changes the bandgap from direct to indirect. 8% of tensile strain completely closes the bandgap giving a semiconductor–metal transition.

Moving on towards ternary tellurides, calculations show HfGeTe₄ (HGT) transitions from an indirect bandgap of 0.67 eV in its bulk form to a direct bandgap of \sim 1.3 eV as a monolayer (Fig. 6(a)) [139]. The higher cohesive energy in 2D HGT (compared to MoS₂, MoTe₂, and HfTe₂) is due to its zigzag-shaped layer and is significant for strong adhesion with metals/insulators, suggesting potential applications of HGT monolayers in electronic devices once fabricated. Monolayers of Ge₂STe and Sn₂STe have not been synthesized to date but their electronic structure has been studied using DFT [137]. They transition to a direct band structure as the thickness is reduced to the monolayer limit. The bandgap can also be tuned by applying an in-plane strain. Fig. 6(b) indicates a semiconductor-to-metal transition at high compressive biaxial strains in Ge₂STe and Sn₂STe monolayers. An indirect-to-direct transition of bandgap is also observed in monolayer ZrGeTe₄, a layered anisotropic semicon-

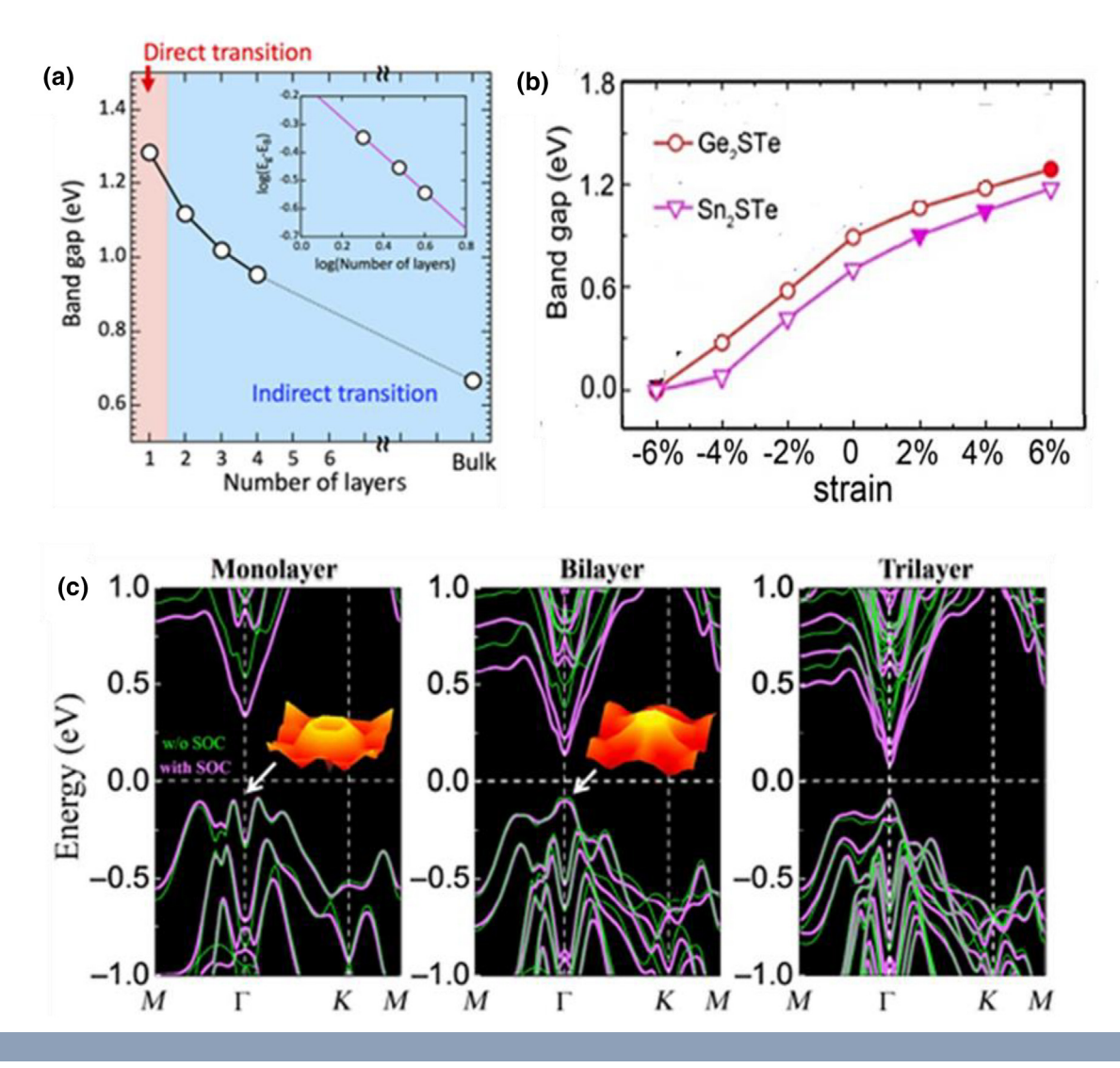


FIGURE 6

(a) Plot of bandgap as a function of the number of layers for HGT [139]. ZGT has a similar plot [186]. (b) The bandgap of Ge_2STe and Se_2STe monolayers under the biaxial uniform strain [137]. (c) Changes in the electronic band structure of layered Se_2Te_4 as a function of the thickness (Inset shows the VBM over the Brillouin zone with SOC) [132].

ductor [186]. The phonon dispersions for 1, 2, 3 layers and bulk ZrGeTe₄ do not show any imaginary frequencies, predicting the stability of layered ZrGeTe₄. Based on the calculated phonon spectra, ultra-thin 2D ZrGeTe₄ has potential applications in nanoelectronic devices due to the anisotropic electrical and optical properties [164].

In most cases, the bandgap changes from indirect to direct when transitioning from bulk to monolayer. However, the calculated electronic band structures for different thicknesses of layered $SnSb_2Te_4$ (SST) with and without SOC (Fig. 6(c)) show an indirect-to-direct transition of the bandgap as the thickness increases from ML to bilayers (BL) [132]. It has been also reported that compared to ML, BL show superior electronic transport properties. The weak anisotropic mobility in the case of ML is also higher in BL. 2D SST is predicted to have high mobility $(27.82\times 10^3~{\rm cm}^2~{\rm V}^{-1}~{\rm s}^{-1}).$

Bulk Nb₂SiTe₄ (NST) is a layered material with a monoclinic crystal structure [141]. Few-layer NST, fabricated using the scotch-tape exfoliation is an intrinsic p-type semiconductor with

a narrow bandgap of 0.39 eV. Measurements reveal that the electron and hole current are equal, making it ambipolar. There is a high charge carrier mobility of $\sim 100 \text{ cm}^2 \text{ V}^{-1} \text{ s}^{-1}$. Zhang et al. [142] predicted that Nb₂SiTe₄ monolayers are ferroelastic and it is possible to tune the anisotropic electronic properties, including anisotropic carrier mobility and optical properties, through ferroelastic switching. Indirect-to-direct bandgap transition can also be achieved by other means, in addition to the reduction in dimensionality. In 2D GaGeTe, the indirect bandgap changes to a direct one under compressive strains of around 2%. A remarkable decrease in the bandgap has been observed when the applied strains are increased. The bandgap decreases as the number of layers (N) increases: $E_g = 0.75$ eV for N = 1 (semiconducting state), whereas $E_g = 0.002$ eV for N = 10 (an almost metallic state) is observed for bulk GaGeTe. DFT calculations suggest that the bandgap of GaGeTe ML can also undergo an indirectto-direct transition under the application of an electric field of 0.11 V Å^{-1} . Increasing the electric field to 0.43 V Å^{-1} can induce a semiconductor-to-metal transition [133-136]. In addition to a

tuneable band structure, 2D GaGeTe also has high mobility of $7.83 \times 10^4~\text{cm}^2~\text{V}^{-1}~\text{s}^{-1}$ for the p-type majority charge carriers [135,136] and exhibiting Rashba effects [134].

Optical and optoelectronic properties

2D tellurides have strong light-matter interactions making the study of their optical properties interesting. $MoTe_2$ and WTe_2 , due to the presence of type-II fermions, have an elliptical Fermi surface. This gives them properties very different from conventional 2D materials. Electronic transport in WTe_2 can be controlled by optical manipulations. The material has an anisotropic bonding: the transmission probability of an optically excited electron was large along the b-axis leading to small distortion of electron transport. Breaking of inversion symmetry produces a higher conductance along b-axis as compared to a-axis [187]. Confinement of the current to the anisotropic direction can be exploited for applications in optoelectronics such as electron beam collimation and electron lenses.

Graphene is a highly promising candidate for wideband, highspeed photodetectors. However, despite its wide band absorption and high carrier mobilities, a weak photoresponse and low external quantum efficiency limits its applications [188]. 2D Gachalcogenides show improved photoresponsivities. Photodetectors made of GaS on Si/SiO2 and PET substrates outperform a lot of 2D materials-based devices, including graphene and MoS₂ [188]. Similarly, photodetectors fabricated of multilayer GaTe also exhibit high photoresponsivity of 10⁴ A W⁻¹ along with photoresponse time of \sim 6 ms at a wavelength of 532 nm. These values are one of the highest among the reported phototransistors made of 2D materials. Compared to GaS, the photoresponsivity of GaTe is higher by an order of 2. This is primarily because of the structural differences between GaTe and GaS (also GaSe). While all the Ga-Ga bonds in GaS (and GaSe) are perpendicular layer planes, in GaTe, only two-thirds of the bonds are normal and the other third are parallel to the planes. This gives GaTe unique properties, such as a direct bandgap of 1.6 eV (while GaS and GaSe have indirect bandgaps above 2.0 eV) which is extremely advantageous for optical and optoelectronic applications [189]. It has an in-plane optical anisotropy in the visible range of the electromagnetic spectrum [190]. Another study on phototransistors of GaTe nanosheets show ultrahigh photoresponsivity of 274.3 A W^{-1} and detectivity of $\sim 4 \times 10^{12}$ Jones for the illumination source wavelength of 490 nm. The GaTe phototransistors can also be integrated into touch sensitive panels, image sensors and solar cells [191]. They can also be used in solar cells, radiation detectors, and nonlinear optics. 2D GaTe has lots of surface defects which also enhance its optical properties. The defects provide a lot of recombination sites for excitons resulting in a photoluminescence emission spectrum in the visible region (480–700 nm) [192]. Another III-telluride, In₂Te₃, has high absorption coefficient making them good candidates for photodetectors and parameter random access memory (PRAM). As the exposure time of the sample is increased at RT, the resistance does not significantly increase, but at lower temperatures, the value almost doubles [155]. Examination of the 2D hexagonal monolayer of SnTe using DFT calculations predicted that its monolayer is a stable quasi-direct semiconductor. It was found to have a strain tunable bandgap of $\sim 1.25-2.00$ eV [193]. Additionally, it has strong absorbance in visible and IR spectral regions [194], making it ideal for IR optoelectronic applications.

The ternary telluride 2D NST is also an excellent candidate for optoelectronic devices. Responsivity measurement for 2D NST-based FETs provides photocurrent of $\sim 1~\mu A$ and an extremely fast response with a 310 μW laser, 532 nm wavelength of laser pulses, 50 mV source-drain bias, and zero potential gate. In contrast, responsivity measurements in mid-IR, with laser power of $\sim \! 160~nW$, laser pulses of $\lambda = 3.1~\mu m$, and a source-drain bias of 50 mV, a photocurrent of 100 nA is obtained, which is higher than the reported values of BP [141]. These properties suggest that the 2D NST could hold a promising future in ambipolar devices and mid-infrared detection. Theoretical calculations on MLs of Ge₂STe and Sn₂STe predict a strong anisotropy in the low energy range (less than 10 eV) and large absorption coefficient (more than $10^5~cm^{-1}$), also indicating possible optoelectronic applications [137].

Ultrafast and nonlinear photonics is one of the applications of layered materials. The Supporting Information briefly discusses the nonlinear properties in 2D materials [195-198]. Tellurene is known to exhibit nonlinear optical response (nonlinear refractive index, $n_2 = 10^{-5} \text{ cm}^2 \text{ W}^{-1}$), with particularly strong Kerr nonlinearity [199]. These results will make the use of 2D Te as nonlinear photonic diodes for telecommunications and alloptical switchers possible. The TI Bi₂Te₃ also show broadband, ultrafast, third order nonlinearity. The n2 of multilayer Bi2Te3 was measured to be 10^{-11} cm² W⁻¹, which is close to that of Bi₂-Se₃. TIs in general have good nonlinear saturable absorption properties even in their bulk form. The monoclinic α-As₂Te₃, which has similar lattice parameters to Bi₂Se₃, is considered one of the best thermoelectric materials [200]. It is equally promising in the field of photonics. Its nonlinear absorption coefficient is predicted to be larger than Bi-chalcogenides. The saturable absorbers manufactured using α-As₂Te₃ cover a wide bandwidth from 1.5-1.9 μm , which can be expanded to 3.7 μm [200]. GaTe also shows interesting nonlinear optical properties. The broken inversion symmetry of GaTe allows it to have a second harmonic generation. Both the second and third-order nonlinearities are not dependent on the number of layers, unlike MoS₂ where the nonlinear optical coefficients decrease with increasing thickness [201]. Due to these properties tellurides can be expected to have a large impact in the telecommunications industry.

Electrochemical properties

Recently, 2D tellurides find applications for their electrochemical properties [202–206]. Cobalt is a transition metal showing multiple oxidation states (Co²⁺, Co³⁺, Co⁴⁺) and has a high reduction potential. These properties of Co along with the large number of active sites for ion migration between the layers in 2D systems, 2D CoTe and CoTe₂ hold potential for supercapacitor applications [110,206]. The electrochemical measurements show improved charge storage and excellent capacitance retention capability in them (Fig. 7(b)) [206]. Bulk CoTe₂ also exhibits electrocatalytic properties [108]. Its nanosheets (Fig. 7(a)) show excellent electrical conductivity and breakdown current density as high as graphene nanoribbons [110].

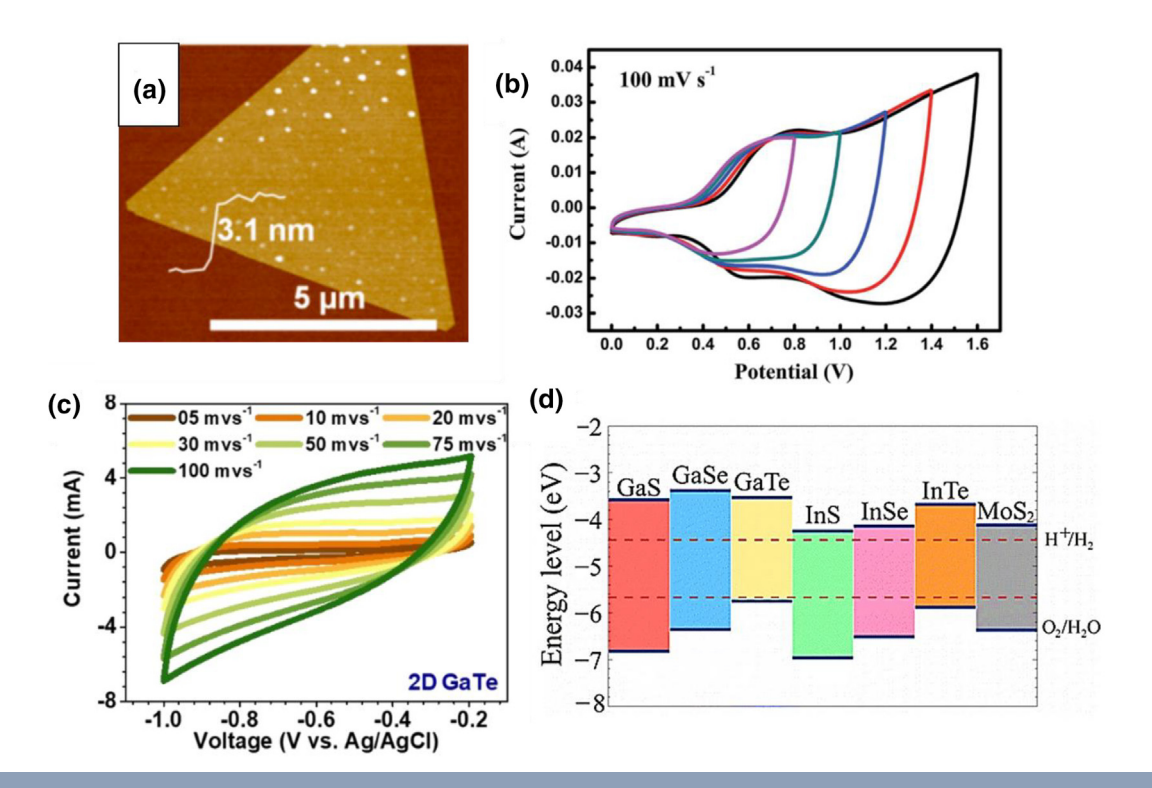


FIGURE 7

(a) AFM image of $CoTe_2$ nanosheet [110]. (b) CV curves of CoTe asymmetric supercapacitors at different potential windows at 100 mV s⁻¹ [206], (c) CV curves of 2D GaTe with 14 F g⁻¹ specific capacitance at 10 mV s⁻¹ [192]. (d) Band edge positions of single-layer materials relative to the vacuum level at zero strain [180].

Among other TMTs, the surface properties of PtTe₂ are also extremely interesting. Platinum itself is an important catalyst in many inorganic and organic reactions. Bulk PtTe₂ is a chemically inert material. However, DFT calculations show that the monolayers of structured 1T-PtTe₂ (Pt₄Te₇) show excellent catalytic activity for hydrogen evolution reaction (HER) [202]. PtTe₂ also demonstrates a high hydrophobicity with a water contact angle of 117°. This value is much higher than the other 2D chalcogenides (98° for MoS₂ and 83° for WS₂) and is a result of the presence of holes on the surface. This contact angle does not change with the thickness of the 2D PtTe₂, demonstrating the intrinsic nature of the hydrophobicity [203].

Studies pertaining to gas sensing show GaTe as a promising material. DFT studies investigated the optical properties and adsorption capability of gas molecules on GaTe monolayer and reported that adsorption energies are favorable for binding with NO₂ and SO₂ gas. The adsorption of the molecules reduces the bandgap as compared to pristine GaTe but improves the absorption coefficient drastically. The values in the case of 2D GaTe are close to the absorption coefficients of lead-halide perovskites. The loss function and reflectivity of the adsorbed material are also enhanced, especially in the UV region [204]. Recently, the possibility of using 2D GaTe in mechanically-flexible supercapacitors was explored. The material shows a ~96% charge retention even after 10,000 charge-discharge cycles, indicating high material stability. Its specific capacitance of 14 F g⁻¹ at a scan rate of 10 mV s⁻¹ is the highest amongst the 2D chalcogenides, demonstrating its promise for applications of energy storage devices (Fig. 7(c)) [192]. Another group III-Te compound, InTe is predicted to show a photo-absorption better than other InZ (Z = S, Se) MLs. A comparison of band edge positions of mono-layered relative materials is shown in Fig. 7(d) [96]. In addition to water splitting, 2D layers of InTe can also be used as photocatalysts. This becomes possible because of the large surface area and reduction in the "distance" to the reaction sites that the photogenerated electrons and holes need to travel, reducing the probability of recombination [205].

Magnetic properties

Intrinsic magnetism in 2D materials was not known until recently. Magnetism in 2D materials have been traditionally introduced using defect engineering, surface functionalization, doping, and straining [24,207]. In 2016, with the discovery of intrinsic magnetism in $Cr_2Ge_2Te_6$ and CrI_3 , the possibility of the existence of 2D ferromagnets was confirmed. Following this, other 2D materials exhibiting magnetism like MnSe₂ [28], $Cr_2-Ge_2Te_6$ [23], VX_2 (X=Se, Te) [24], Te_3GeTe_2 [27], $TePS_3$ [25], and TeTe [26] were synthesized.

Complex structures of the form $CrXTe_3$ (X = Si, Ge, Pb) are ferromagnetic semiconductors, and form when the high-spin state of S = 3/2 for a Cr^{3+} ion ferromagnetically couples to the three nearest Cr^{3+} ions [127]. Single crystals as well as MLs of $CrSiTe_3$ are intrinsically ferromagnetic. DFT studies show that the cleavage energy for $CrSiTe_3$ is 77 meV/atom, lower than that of MoS_2 (43.7 meV/atom). Resultantly, monolayers of $CrSiTe_3$ can be obtained by scotch-tape exfoliation [208]. This, however, makes the measuring the thermal conductivity along c-axis challenging. In the ab plane, the thermal conductivity (κ_{ab}) of paramaging.

netic CrSiTe₃ shows phonon glass behaviour. The low κ_{ab} at RT further decreases as the temperature is decreased. However, as the temperature crosses T_{c} , κ_{ab} increases rapidly and peaks at 8 K. This implies that the glassy behaviour is a result of phonon scattering by magnetic fluctuations. Even below T_{c} , the conductivity remains significantly lower than those of crystalline solids, indicating the strong spin-lattice coupling in CrSiTe₃ that keeps the phonon thermal conductivity from fully recovering below the Curie temperature [209]. Their ferromagnetic-antiferromag netic (FM-AFM) transition, bandgap variation (Fig. 8(a)), and the nearest neighboring Cr-Cr distance can be tuned by applying external elastic strain [127,128]. In bulk form, it is difficult to introduce large elastic strains because of the high plasticity in materials. The plasticity is limited due to nanostructuring allowing us to apply elastic strains [127]. Antiferromagnetism in CrSiTe₃ arises when the Cr-Cr distance is reduced (applying compressive strain), while ferromagnetic behavior is observed when this distance increased. Increasing the strain increases the stability if its ferromagnetic state while preserving the semiconducting behavior (Fig. 8(b)). By applying a tensile strain of 8%, the $T_{\rm c}$ increases to 290 K [127]. This shows CrSiTe₃ ML has potential applications in spintronic devices at RT.

The single crystals of $CrGeTe_3$ are also ferromagnetic semiconductors, exhibiting an indirect bandgap and T_c of 61 K, which is higher than $CrSiTe_3$ (32 K) [96]. $CrGeTe_3$ has a smaller vdW gap (3.3 Å) than $CrSiTe_3$ (3.32 Å) [129]. Both $CrGeTe_3$ and $CrSiTe_3$ have large magnetic anisotropy energy (MAE), which stabilizes the magnetic order at finite temperatures and overcomes the thermal fluctuations [210]. Fig. 8(c) shows the effect of strain on 2D $CrXTe_3$ (X = Si, Ge). Heisenberg model-based Monte Carlo simulations predict that the T_c of ML $CrGeTe_3$ ($CrSiTe_3$) nanosheets increase from 57.2 (35.7) K at the equilibrium state to 108.9 (91.7) K under 5 % strain [129]. Adsorption of hydrogen or alkali metal ion (Li, Na, K) on the surface of the unit cell (at the top of Cr atom) can alter the electronic/magnetic properties of the isostructural $Cr_2Ge_2Te_6$ (Fig. 8(d)). With adsorption of the

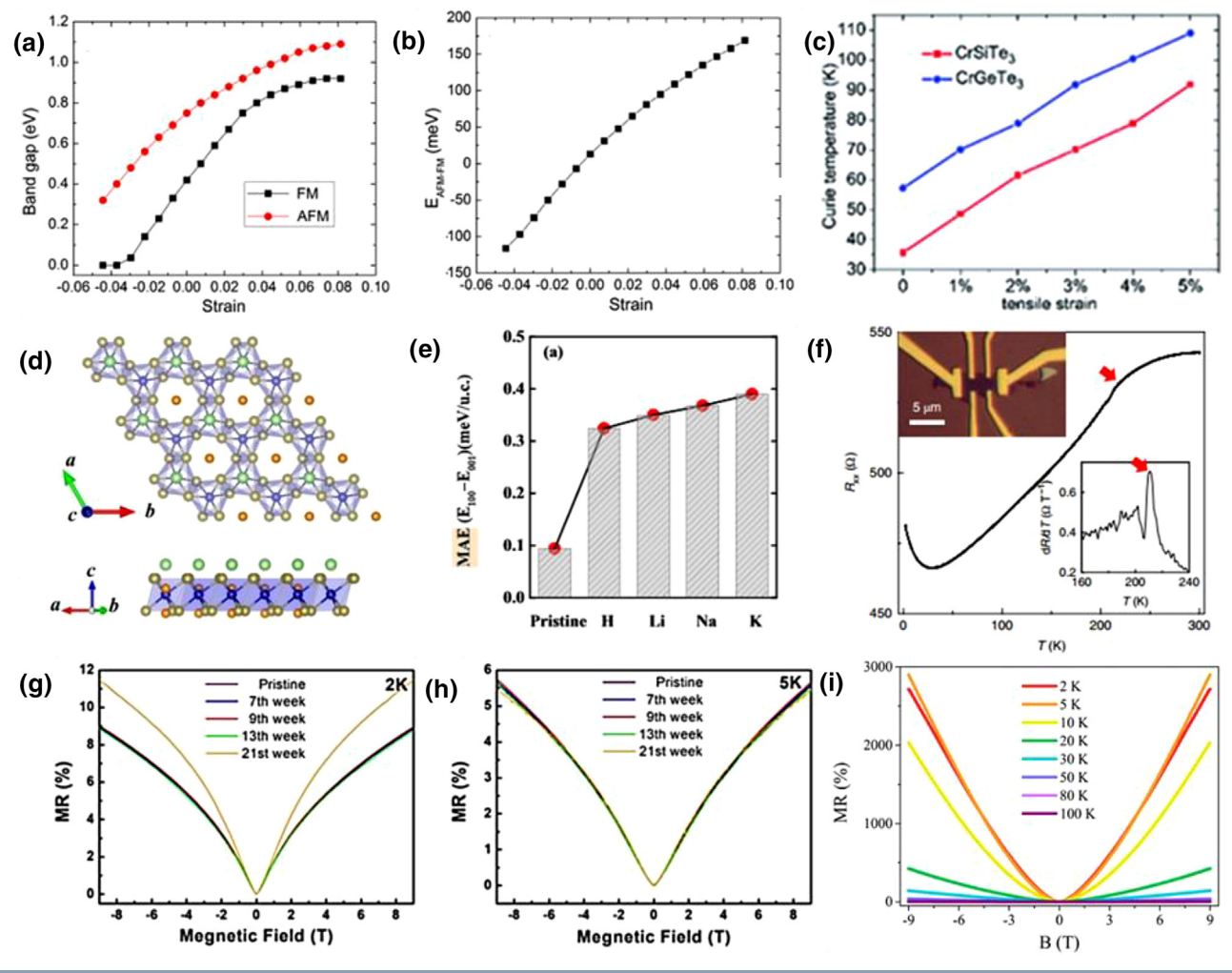


FIGURE 8

(a) Variation of bandgap values with applied strain for FM and AFM configurations [127] (b) The energy difference between AFM and FM configurations (E_{AFM-FM}) varies with the increase of strain. A positive E_{AFM-FM} indicates the stability of FM over AFM configurations [127]. (c) Plot showing the effect of applied tensile strain on Curie temperature for CrSiTe₃ and CrGeTe₃ [129]. (d) Adsorption configurations of $Cr_2Ge_2Te_6$. (e) A bar chart showing the variation of MAE in pristine monolayer $Cr_2Ge_2Te_6$ and with H, Li, Na, and K adsorption. The magnitudes of the MAE increase with the increasing size of the adatom [210]. (f) The temperature-dependent longitudinal resistance for 12 nm thick FGT device. The upper-left inset shows an optical image of the Hall bar device. The bottom-right inset shows the first derivative of the longitudinal resistance as a function of temperature [123] MR at $\theta = 90^{\circ}$ with different exposure time in ambient air at (g) 2 K and (h) 5 K [155], (i) MR vs magnetic field || c-axis at a selected temperature [104].

H atom, a magnetic moment appears in Cr because the adatom H redistributes charges around neighboring Te atoms, improving the ferromagnetism in $Cr_2Ge_2Te_6$. It however, remains semiconducting with a bandgap of 0.95 eV. But, adsorption of alkali metal pushes the Fermi energy up to the conduction band, turning $Cr_2Ge_2Te_6$ into a ferromagnetic metal. The surface adsorption also leads to an increase in the MAE, hence increasing the T_c (Fig. 8(e)) [210].

Another structurally similar material, CrPbTe₃ (CPT) monolayer, although not fabricated, is predicted to exhibit a ferromagnetic ground state, high $T_{\rm c}$ (110 K) (larger than that of CrI₃, CrSiTe₃, and CrGeTe₃), and in-plane magnetic anisotropy. Because of this anisotropy, properties such as cleavage energy, bandgap, and Curie temperature in 2D CPT monolayer can be tuned by applying strain. A 4% tensile strain increases the $T_{\rm c}$ to 150 K. The CPT monolayers show strain-induced semiconductor-to-metal transition and spin reorientation transition from in-plane to perpendicular magnetic anisotropy under compressive strains.

While all of the above-discussed materials possess intrinsic magnetic order, the Curie temperatures are still extremely low for practical applications. Only with high strains, a T_c of 290 K was achieved in CrSiTe₃. The Fe-Ge-Te system, forms an important category exhibiting intrinsic 2D ferromagnetism having relatively higher T_c (as high as RT) without any strain/dopant. 2D Fe₃GeTe₂ has a strong, perpendicular magnetic anisotropy (PMA) and a high T_c of 230 K [121]. The material has a near square-shaped magnetic hysteresis loop signifying a hard magnetic phase along with a large coercivity of up to 550 mT at 2 K [120,122]. Magnetotransport measurements on thin films of Fe₃GeTe₂ reveal kinks at ~210 K in temperature-dependent longitudinal resistance, R_{xx} -T plots for a 12 nm FGT Hall bar device. The observed kinks in both R_{xx} and its first temperature derivative (Fig. 8(f)) and lower-right inset respectively) demonstrate a magnetic phase transition from paramagnetism to ferromagnetism at that temperature [123]. 2D Fe₃GeTe₂ synthesized by both MBE and exfoliation methods show an antiferromagnetic coupling [124]. A negative remnant magnetization has been observed at 90 K, which indicates the creation of antiferromagnetic coupling (AFC) within the ferromagnetic bilayers. The presence of antiferromagnetism in 2D Fe₃GeTe₂ plays a crucial role in magnetoresistance applications. Due to its unique magnetic properties, it has been suggested for compact low-power spintronics [120,122,124], voltage-controlled magneto electronics [163], and magnetic storage [125] applications. Fe₃GeTe₂ forms trilayer vdW heterostructures with other layered materials such as hBN and graphite [126,211]. Magnetic tunnel junction devices are fabricated as FBT/hBN/FGT which exhibit an ideal tunneling spin-valve behavior. This ideal behavior is a result of the vdW nature of Fe₃GeTe₂ and thus, similar can be expected from other vdW ferromagnetic materials [126]. Another newlyfound ferromagnetic material and a member of the FGT family, Fe₅GeTe₂ has a Curie temperature in the range of 280-310 K (depending on the thickness of the material) [212]. Similar to Fe₃-GeTe₂, atomically thin flakes of Fe₅GeTe₂ can be easily obtained by micromechanical exfoliation. 2D Fe₅GeTe₂ is also excellent candidate for making functionalized vdW heterostructures at RT. DFT calculations show its magnetic

moment increases significantly from 1.65 μ_B to 2.66 μ_B by applying biaxial strains [213]. The strain-tunable nature of magnetism will play an important role in the fabrication of heterostructures. While Fe_5GeTe_2 is similar to Fe_3GeTe_2 in many aspects, their physical properties differ. The PMA in 2D Fe_3GeTe_2 increases monotonically as temperature decreases. However, in Fe_5GeTe_2 , PMA is first observed at 200 K and as the temperature is decreased, it increases to a maximum at 120 K and then decreases [212]. Fe_5GeTe_2 also shows interesting butterfly-shaped magnetoresistance that is thickness-dependent [214].

Magnetoresistance (MR) is the change of electrical resistance of a material due to an externally applied magnetic field and has applications in magnetic storages, sensors, and spintronics. Interesting properties are exhibited by the 2D tellurides in the measurement of MR. In In₂Te₃, it decreases with increasing temperature but does not change with time of exposure (in magnetic field). MR also varies quadratically with increasing magnetic field at 2 K and 5 K due to weak anti-localization effects (Fig. 8(g,h)) [155]. Reports show that in low temperatures, the layered WTe₂ showed extremely large positive MR of 452,700% at 4.5 K in 14.7 T and 13,000,000% at 0.53 K in 60 T, when the current direction was along the tungsten chains and magnetic field perpendicular to the dichalcogenide layers [215]. No indication of resistivity saturation, even at a very high applied field, makes WTe2 a unique material. WTe2 has a small overlap between valence-band and conduction band states along with having excitonic-insulator-like character [216]. Thus, each electron has a corresponding hole, making it a nearly perfectly balanced electron-hole population and giving the highly non-saturated MR at a very high field. When the magnetic field is applied parallel to the electric field, 2D WTe₂ shows a negative MR [217] as a result of chiral anomaly [218] thus, distinguishing type-II Weyl semimetals from the type-I [219]. A fast fourier transform (FFT) of the second-order derivative of MR shows that the frequencies reported are due to quantum oscillations arising from four ellipsoidal Fermi surfaces, two-electron pockets (α and β) and twohole pockets (γ and δ) [220]. The MR in ZrTe₂ deviates from Kohler's rule by showing very high values of MR at low temperatures (Fig. 8(i)). The MR is also larger than most topological insulators.

Mechanical properties

Silicon telluride, Si₂Te₃ has a unique structure that imparts interesting mechanical properties to it. The Si atoms form a Si-Si dimer and fill two-thirds of the metal sites in a hexagonal lattice formed by Te atoms. The dimers have four possible orientations: along the 3 horizontal (in-plane) directions and one out-of-plane direction. Because of the low energy barrier for rotation of the dimers, the Si₂Te₃ has a structural variability [221]. 2D Si₂Te₃ has one of the highest critical strain of 38% above which no phase transformation occurs and has an ideal strength of 8.59 N/m, that is lower than popular 2D materials, indicating an extremely high flexibility for applying mechanical strain to tune properties [222]. The bandgap of the material can be tuned as well as an indirect-direct bandgap transition can be induced by applying mechanical strain.

Defects in a material play a key role in influencing the physical properties of materials. Vacancies directly influence the electronic properties of group IV-tellurides (XTe, X = Si, Ge, Sn and

Pb) [223]. The p-type nature of the group IV-tellurides is due the prominence of X-atom vacancy. A Te-vacancy, on the other hand, converts SiTe from a semiconductor to a semimetal. Moreover, vacancy defects reduce the mechanical strength of XTe monolayers due to smaller elastic moduli.

The tetradymite $\mathrm{Bi_2Te_3}$ is an extraordinary thermoelectric material and a topological insulator. These properties are greatly influenced by dislocations. Low-angle grain boundaries, that arise due to lining up of dislocations, scatter phonons in the mid-frequency range improving the thermoelectric performance of the material [184]. Mechanical strength is also desired in a good thermoelectric material. A composite of graphene oxide nanoparticles (GNP) and MnTe was prepared. Inclusion of 0.25% of GNP improves the mechanical properties, such as fracture toughness by 33%. The inclusion of GNP also improved ZT values, as it reduces thermal conductivity and increases the Seebeck coefficient [185].

 Bi_2Te_3 films on the flexible substrate of indium tin oxide coated PET (polyethylene terephthalate) have also been used in flexible nonvolatile memory devices due to its nonvolatile bipolar resistive switching characteristics and good mechanical flexibility [224]. Even WTe₂ nanosheets when drop-cast on Au/Ti coated PET substrate result in flexible supercapacitors with excellent flexibility and high mechanical strength. The supercapacitors could bend between 0°-90° without much change in the cyclic voltammetry curves [74].

Anisotropy in 2D materials can be exploited to develop direction-dependent devices such as polarized-optics and photodetectors, artificial synaptic devices, and digital inverters. Applying uniaxial tensile strain reveals anisotropic mechanical, electronic, and optical properties in As₂Te₃ nanosheets. The monoclinic nanosheets show more tensile strain along the crystallographic *x*-direction than along the *y*-direction. The reason behind this is the bond elongation along *x*-direction as compared to a coupled result of bond elongation and structural deflections due to a lower elastic modulus along the *y*-direction. The As-Te-As bonds have remarkable stretchability (more than three times that of graphene layers), making these materials ideal for flexible semiconductor applications. Its indirect bandgap increases with decreasing thickness.

Other emergent properties

Topological properties

Quantum states of matter were first discovered in 1980. They are defined in terms of their nontrivial topology of the quantum mechanical wave function. The best-known example of a topological phase is the quantum spin Hall (QSH) insulators, also known as, the 2D topological insulators (TIs). They are insulating in bulk and have two 1D conduction channels in each of the edges, conducting pure spin-current. Bulk Bi_2Te_3 is predicted to be a TI [225] with massless Dirac-like surface states protected by time-reversal-symmetry [226]. The bulk conduction band (CB) is not observed near the Fermi energy (E_F) demonstrating an intrinsic TI behavior. The study of thickness-dependent band structure using Angle-Resolved Photoemission Spectroscopy (ARPES) (Fig. 9(a–d)) shows a single-Dirac-cone surface state forms at two quintuple layers (2QL), and the bulk CB becomes smaller when it goes to 5QL from 2QL [226]. However, an

intense bulk electron pocket comes at the Fermi level because of vacancies and anti-site defects in bulk TIs [227]. Simulations predict that the crossover regime from 3D to 2D with the QSH effect occurs in an oscillatory manner with respect to the layer thickness [228].

The type-II Weyl semimetals are also important topological materials. WTe2 was the first type-II Weyl semimetal to be discovered. It was predicted that eight separated Weyl points exist in bulk WTe2, which are connected by Fermi arcs on the (001) surface. The Fermi arcs are topological boundary states emerging at the surface of bulk Weyl semimetals. The connected Weyl points are of opposite chirality and exist in different Fermi arc lengths [229,230]. 1T'-WTe₂ monolayers exhibit QSH state [231–233]. It exhibits a quantum Hall conductance without the application of magnetic field due to topologically protected, dissipation-less edge states that build an energy gap [234] opened by band inversion and strong SOC. First-principles calculation of 1T'-WTe2 monolayer show topological band inversion, which forms a Dirac cone and leads to a bulk bandgap. The bulk bandgap is a result of symmetry-breaking due to the distorted structure of WTe₂, which lowers the dz^2 orbital below E_F, lifts the d_{xz} orbital near the Γ point, and hybridize the bands due to SOC (Fig. 9 (e)) [231]. Below 100 K, WTe₂ monolayers become insulating in their bulk portion but remain conducting along the edges. This is not observed even among the bilayers [235].

Given that both MoTe₂ (see Section "Electronic and transport properties") and WTe₂ show exceptional topological properties, theoretical studies were carried out to predict the behaviour of MoTe₂ when doped with W. The results indicated a phase change in MoTe₂ from a semiconducting to a metallic state [114]. In fact, $Mo_xW_{1-x}Te_2$ is a semimetal, where the topological Fermi arcs are above the Fermi level. The two Fermi arcs are connected by the same Weyl point and the Fermi arc is not disjoint and looks like a ripple [115]. Later, 2D $Mo_xW_{1-x}Te_2$ (x = 0.09) was fabricated by exfoliating its crystals. The study of $Mo_{0.91}W_{0.09}Te_2$ revealed a semiconductor transition from an indirect-to-direct bandgap of 1.10 eV at the monolayer limit [114].

In IrTe₂, strain can be used to tune the topological properties in 2D semimetals and induce phase transitions. It is a type-II bulk Dirac semimetal with the Dirac point slightly above the Fermi level [149]. It shows multiple phases as the temperature is decreased from RT. At RT, IrTe2 shows a trigonal phase, which changes to monoclinic as the temperature is decreased to 7 The monoclinic structure is also called the $q_{1/5}$ phase where a periodic $5 \times 1 \times 5$ structure is formed. The transition follows first-order kinetics. The ordering kinetics is dependent on the thickness of the thin-films: the transition slows with decreasing thickness. A metastable superconductive state is realized due to supercooling by virtue of thinning [236]. As the temperature is further decreased to -93 , a new periodic phase, $q_{1/8}$ is formed with $8 \times 1 \times 8$ structure [237]. In addition to these, a lot of degenerate low-temperature phases exist at the surface of IrTe₂. It has a strong SOC which gives it properties such as CDW and superconductivity. The 6×1 phase of the material has been stabilized by applying uniaxial tensile strain [149]. A tunable superconducting behavior has also been predicted under a uniaxial compressive strain. These properties make the material suitable for applications in memory, oscillator, and superconductor

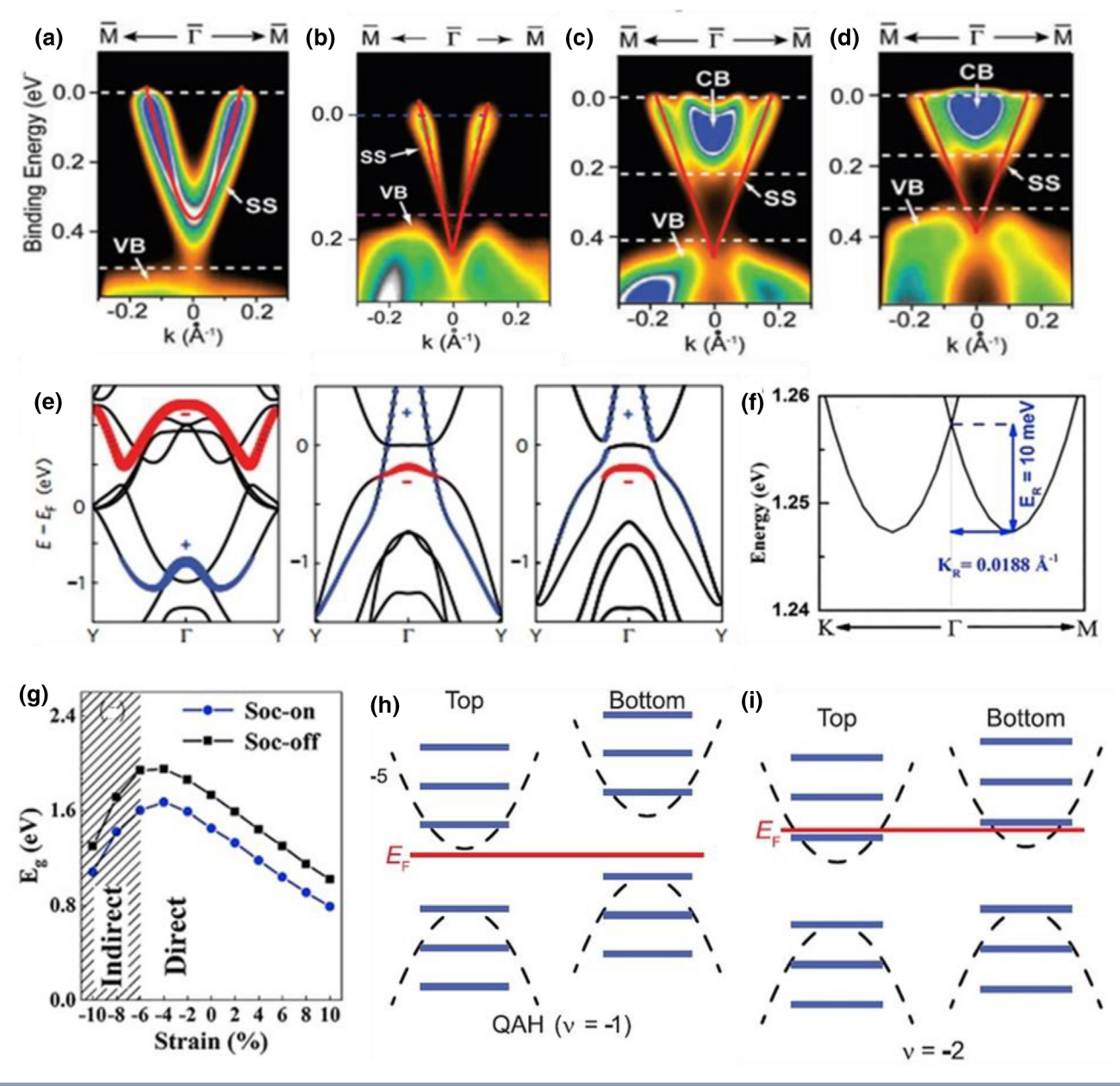


FIGURE 9

(a) Band structure of ultrathin films of Bi_2Te_3 using ARPES intensity maps 1QL (b) bulk (c) 2QL (d) 5QL [226]. (e) Calculated band structures for WTe₂ to show the evolution from 1T-WTe₂ along the 0–Y direction [231]. (f) The magnified view of the Rashba spin splitting of InTeF at CBM, (g) Variation of E_g as a function of strain for InTeF [138]. Schematic band diagrams for the top and bottom surface states of the 5-layer MnBi₂Te₄ sample. Dashed parabolas denote surface bands under zero magnetic field. The bands collapse into LLs (blue horizontal lines) under an external magnetic field. Red horizontal lines represent Fermi level E_F that is tuned by the backgate in our experiment. (h) and (i) display the band configurations of the observed n = -1 and n = -2 states, respectively [239].

devices. Alloying it with tantalum yields TaIrTe₂, which is a unidirectional noncentrosymmetric type-II Weyl semimetal and was recently synthesized. A slightly tilted Dirac cone was observed in its electronic structure implying anisotropic spin transport properties and possible application as an information storage unit [238].

 $MnBi_2Te_4$ is another TI that has been widely studied. A phenomenon called layer magnetization has been observed where they exhibit magnetic states in odd-layer flakes under vertical magnetic fields. Samples with an odd number of layers, e.g., 3 and 5 layers become ferromagnetic while a 4-layer sample

remains antiferromagnetic. Fig. 9(h, i) shows the band diagrams for the top and bottom surface states of this 5-layer sample. This can be attributed to the substrate-induced disorders or asymmetry in the sample [239]. In a similar study, single crystals of MnBi_2Te_4 were seen to exhibit magnetic order below 25 K which was a result of antiferromagnetic interactions between Mn layers and topological quantum states [240].

Phase transitions

The different topological phases are classified according to their electronic band topological indices. Some materials possess phases that are topologically completely different. The most studied materials for such phase transitions are the Mo- and Wchalcogenides. As already discussed, these materials possess two stable phases that are competing in energy, viz., 2H and 1T'. In the 2H phase, TMTs are semiconducting with a topologically trivial band structure while in the 1T' phase, they are topologically insulating. Since the differences between the phases are due to different stacking arrangements, the transformation is diffusionless and martensitic in nature [241]. The transition is from a nontrivial topological phase to a trivial one, with a high energy barrier, giving both the phases long term stability and hence making them suitable for applications in data storage devices. Multiple techniques have been proposed to facilitate the transition from a 2H to a slightly less stable 1T' such as: laser irradiation, and ionic liquid gating. However, these methods are not perfect. Not to mention, the fabrication of 1T' phase itself is difficult. Zhou et al. proposed, based on DFT calculations [241], the use of a laser of terahertz frequency to illuminate TMDs, which would lead to ultrafast transition between 2H and 1T' phases. The proposed method is contactless, athermal and nondestructive/non-invasive.

Ultrafast phase transition induced by THz illumination has also been observed in the Ge-Sb-Te (GST) alloys which are widely used in optical drives. GST are phase change materials, existing in amorphous and crystalline phases with the transition between them being ultrafast (within 10^{-8} s). The amorphous regions of the optical disks store the data. The use of laser crystallizes the illuminated regions overwriting the data by heating the parts of the disk above glass-transition temperature. Materials in the GST family include $GeSb_2Te_4$, and $Ge_2Sb_2Te_5$ [242]. Doping Sb_2 -Te also produces a material similar to GST that show good optical contrast. Typical dopants include Ge, In and Ge, In fact, Ge0 has being used in rewritable optical drives (DVD-RW) [243].

Electrostatic gating has been recently identified to induce structural phase transition from semiconducting (2H) to a semimetallic phase (1T') in monolayer MoTe₂. A certain surface charge density is required, in presence of stress, for such a transition. The gate voltage however is very close to the breakdown voltage of 2H MoTe₂ that can potentially cause problem in a laboratory/industrial setting. Alloying with W to form $Mo_xW_{1-x}Te_2$ can reduce the required gate voltage [244]. The dynamic control of structural phase transitions through gating is a novel mechanism that is not available for bulk materials. In 2D forms, the 2H phase is more stable compared to 1T', that is, the energy states in 2H are lower than the 1T' phase. The excess electrons introduced in the 2H phase of the material under electrostatic bias increase the total energy of the 2H phase; as a result, the ground state switches from 2H to 1T', leading to a phase change. This transition is purely structural resulting in a different crystal structure and is different from the CDW transitions in TaS2 and TaSe₂ due to gate doping [245]. The structural phase transition in MoTe₂ and Mo_xW_{1-x}Te₂ through electric-field can be used in resistive random-access memory (RRAMs). For this, instead of transitioning from 2H to 1T', a transient state 2H_d is chosen. The 2H_d phase shows behaviour ranging from semiconducting to metallic, and in general, is more conductive than 2H. Due to this, devices manufactured out of these two materials can be reversibly transformed between a high resistive state to a low

resistive state, hence giving the working principle behind RRAMs [246].

One of the most widely used method to induce phase transformation is strain engineering. Our discussions this far show strain can be effectively used to tune properties like magnetism, and electronic band structure in few materials. Strain modulated phase transition has been extensively studied for MoTe₂. A tensile strain of 0.2% can lower the 2H-1T' transition temperature down to RT. This transition is homogenous and reversible. Since such a transition is associated with a large decrease in resistance, MoTe₂ can be used to develop extremely sensitive sensors [247]. Furthermore, Hou et al. explored electric-field induced strain that reversibly transforms MoTe2 between its two phases for FETs [248]. Moreover, the TeSe₂ monolayer, which was developed as an isoelectronic compound of the tetragonal form of Te, was found to be stable and exhibit three structures HyT, MH, and $M\beta\alpha$. The HyT and $M\beta\alpha$ phases adopt a layered structure. The three forms can be transformed into one another under the application of uniaxial tensile or shear stress [144].

Phase transition can also be induced by thermal treatment and chemical doping. The former involves irradiating 2H-MoTe₂ with laser that thins the MoTe₂ flake and induces a transition from 2H to 1T'. This is different from the martensitic displacive phase transition discussed above. The phase transition, in this case, is triggered by the evaporation of Te atoms due to irradiation. Cho et al. deposited 2H-MoTe₂ on top to form a heterophase homojunction that is stable at 300 [249]. The carrier mobility of this transistor was found to be 50 times that of transistors of MoTe₂ as a perfect ohmic contact is achieved in this case. Chemical doping too can be employed for phase engineering. In WTe₂, by substituting the Te atoms with S or Se to form WSe_{2(1-x)}Te_{2x}, the 1T_d metallic phase can be transformed into the 2H phase [250].

Rashba effects

The Rashba effect is the splitting of the spin bands in crystals. The presence of heavy atoms in a crystal leads to a spin-orbit coupling (SOC), which results in shifting of the VBM and CBM from their symmetry points in the Brillouin zone. The two discussed compounds of the Se-Te system (SeTe and TeSe2), in addition to having excellent electronic and optical properties [251,252], form a topological insulator with Rashba SOC and band topology [160]. The electronic structure of buckled SeTe also reveals a Rashba-like splitting of bands near the Dirac cone. First-principles calculations show anisotropic band dispersions near the Fermi level. A Dirac-semimetal state exists because of the anisotropic band dispersion, inversion symmetry, and a significant SOC. Dynamical stability at T = 0 K is predicted in the SeTe ML without any soft phonon modes and is predicted to maintain its structural integrity at RT. In the presence of strain, from -5% to 1%, the bandgap decreases, closing entirely at 1% and then again increases from 1% to 5%. Thus, there is a topological phase change at 1% strain. In crystals lacking an inversion symmetry or noncentrosymmetric materials, the electronic energy bands are split by SOC. An essential feature of SOC is that the electrons moving in the electric field, experience magnetic force even in the absence of an external magnetic field [253].

Rashba effect is also predicted in MLs of fluorinated InTe. They are stable, functionalized structures having a large Rashba spin splitting of about 1.08 eV Å with the splitting energy (E_R) of about 10 meV (Fig. 9(f)), which is amongst the largest reported in 2D materials [254]. The Rashba effect allows the material to be tuned by applying an electric field, making it ideal for spintronics devices like spin FETs. 2D InTeF monolayer also has a tunable direct bandgap. The bandgap changes between 0.78 to 1.67 eV with the application of strain from -10% to 10% (Fig. 9(g)) [138]. It is also predicted that the Rashba effect and the direct bandgap characteristics of the monolayer would be retained on a substrate, thus making the fabrication of heterostructures possible.

Superconductivity

Iron telluride (FeTe) is a parent compound for many Fe-based chalcogenide superconductors. It has an antiferromagnetic ordering below 70 K, which becomes superconducting with Tesite doping [117]. Fe-based superconductors have high superconducting transition temperatures (up to 56 K at ambient pressures). The material has a high magnetic moment. Its susceptibility increases with decreasing the temperature below 300 K but decreases drastically at 70 K, as shown in Fig. 10(a), due to coupled magnetic and structural changes to the orthorhombic phase [117,118]. Electrical conductivity shows a similar pattern - it increases with decreasing temperature and then suddenly decreases below 70 K [117]. Fe_{1+v}Te bulk crystals are grown by the self-flux method [119]. Properties of its thicker flakes (>30 nm) are similar to bulk samples. With the transformation from paramagnetic to antiferromagnetic at 62 K, a structural phase change is observed from tetragonal to orthorhombic. For intermediate thickness, there is a semiconducting phase transition at 10 K. The reasons for the appearance of superconductivity in FeTe flakes are - (i) change in Fe-Te-Fe bond angles because of tensile strain, (ii) oxidation, which changes the Fe 3d valence state and suppresses the local magnetic moment. For even thinner flakes, the material exhibits insulating properties and an enhanced MR at low temperatures. As the thickness decreases, the nanoflakes begin to behave like a highly disordered 2D system, exhibiting localized states, with positive MR at low temperatures.

Other TMTs like TiTe2, NbTe2, and PdTe2 also exhibit superconductivity. TiTe2 is a semimetal, but under high pressure, it can act as a superconductor. The superconductivity emerges with phase change from hexagonal to monoclinic at 5.4 GPa and becomes robust at 50.2 GPa. At ambient pressure, the hexagonal TiTe2 is hole-dominated, but after the phase transition (at 19 GPa), the majority carriers change to electrons. Fig. 10(b) shows the temperature-pressure phase diagram indicating the metallic, weakly localized, and superconducting phases [102]. A unique free charge carrier and phonon-coupling lead to the emergence of CDW and superconductivity in NbTe₂. This arises during the synthesis of NbTe2 where it experiences a reduction of dimensionality. It has been observed that the superconducting transition of this material occurs at 0.5 K and that it depends on the current density. PdTe2 shows superconductivity below the critical temperature of 1.7 K. ML 1T-PdTe2 is a narrow bandgap semiconductor. Two MLs is the critical thickness where the

vdW coupling is feasible and the material transitions to a metallic phase. A transition to type-II thin-film superconductivity is also observed from type-I bulk superconductivity below a critical thickness of 10 MLs [97]. Fig. 10(c) shows a comparison of the transition temperature of a few superconducting tellurides, and it can be clearly seen that FeTe-based superconductors outperform the others.

Charge density waves

TiTe2 has interesting structural and electronic properties, particularly, its 1T polytype. It is considered a textbook example of Fermi liquid and shows a charge density wave (CDW) phase transition at 92 ± 3 K on cooling, which is not observed in bulk material and bilayers. The CDW state is a quantum state of periodic modulation of the electronic charge density along with a periodic distortion of the atomic lattice [106]. CDW in TiTe2 was unexpected because DFT calculations did not show any tendency to distort towards a 2×2 CDW structure. The transition occurs, however, at a lower temperature of 100 K compared to other similar materials like TiSe2, indicating that the driving force for distortion is considerably weaker in TiTe2 [101]. The reason speculated was the higher tensile strain of ML stabilizing the CDW distortion. VTe2 also exhibits a CDW state. The CDW transitions were studied, and two associated phase changes were observed one corresponding to two resistance switching states (Fig. 10(d)), and the other to, two pronounced Raman blue shifts. These phase transitions can be switched and controlled by electric-field and thus, find applications in memory devices [106]. The magnetic ordering in the VTe₂ shows a very high magnetoresistance and a perfect spin Seebeck effect, making it ideal for applications in spintronics and quantum devices [107].

Semimetallic 2D ZrTe₃ also exhibits CDW transitions. The crystal structure of the ZrTe₃ has "infinite" rods of ZrTe₃ prisms stacked into a chain along the b-direction. This is related to the prototypical NbSe₃ crystal structure. However, because of the CDW transition at 63 K, the conduction properties deviate from typical NbSe₃ type materials. There is a gap in the Fermi surface (FS) in the CDW state due to the formation of electron-hole pair with wave vector \mathbf{q}_{CDW} , which leads to the nesting of a portion of FS with another. This gapping induces anisotropy in many properties of the material, including electrical resistivity [255]. It was observed that with increasing pressure, \mathbf{q}_{CDW} changes its values, and above 5 GPa, the CDW state abruptly disappears [256]. There is also the appearance of superconductivity beyond 5 GPa. Superconductivity arises because the charge carriers that went into stabilizing the CDW state becomes available.

Rare-earth tellurides (R-Te) form a family of quasi-2D CDW compounds. The CDW transition temperature ($T_{\rm CDW}$) varies with the mass of the rare-earth element; lighter rare-earth elements show only one CDW order $\sim\!300$ K, whereas the heavier elements show a second one at a lower temperature. In R-Te, there is always a feud between superconductivity and CDW. Since both these quantum phenomena are a result of electron–electron and electron–phonon interactions, when one dominates, the other is suppressed. Superconductivity can be achieved by suppressing the CDW in these materials using high pressure. At high pressures, the CDW state of GdTe₃ is suppressed and shows superconductivity at low temperatures [161,257]. At 5 GPa, it

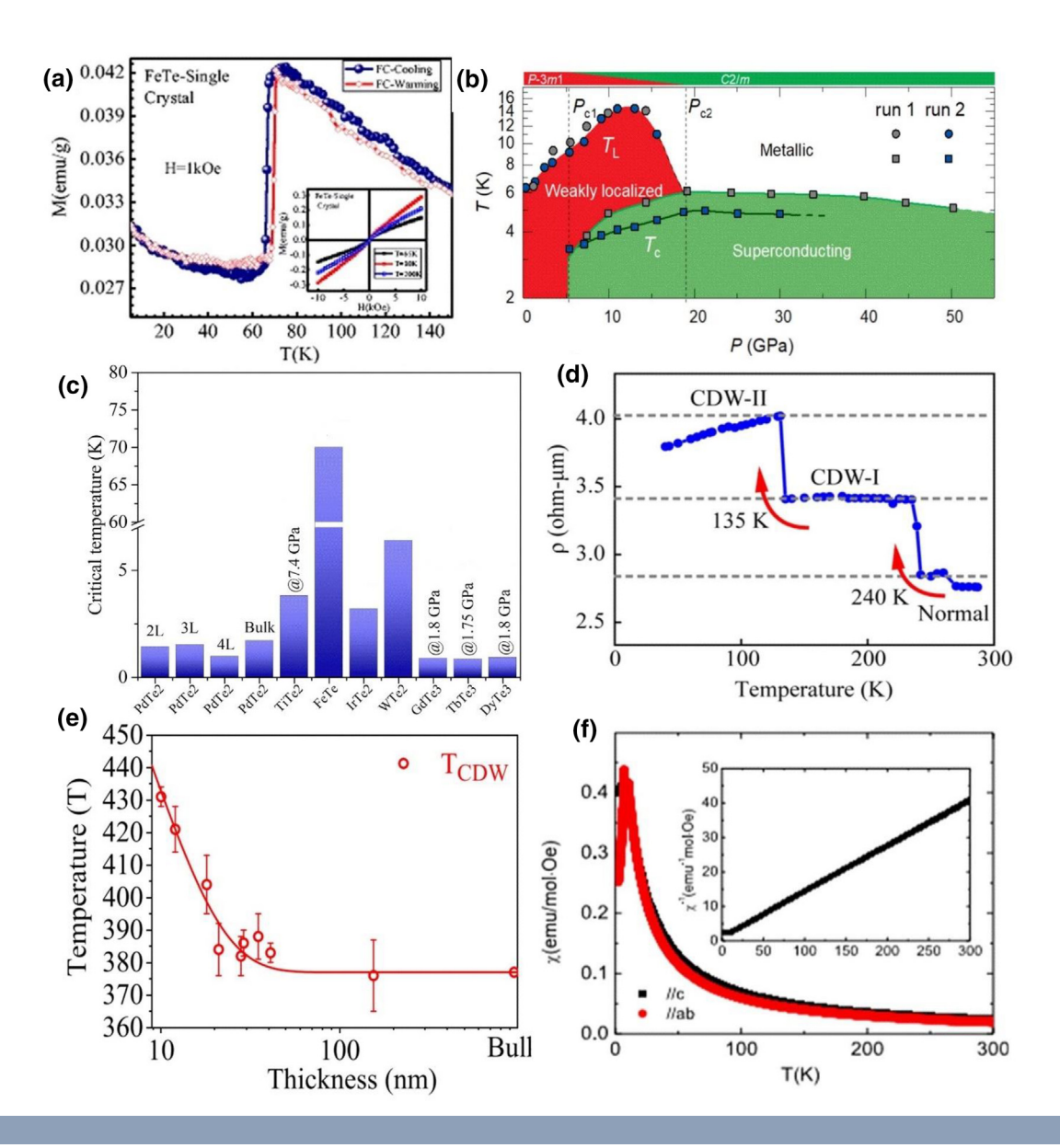


FIGURE 10

(a) The DC magnetization plots for the single-crystal of FeTe, measured in the applied magnetic field of H = 1 kOe [117]. (b) Temperature-pressure phase diagram of TiTe₂ [102]. (c) A comparison of the critical temperatures (T_c) of some 2D tellurides showing superconductivity [97,102,117,118,236,257,258], (d) Temperature-dependent resistivity of 7 nm thick film exhibiting two abrupt jumps corresponding to CDW phase transitions at 135 and 240 K [106]. (e) Thickness dependence of T_{CDW} in GdTe₃ [161]. (f) The temperature dependence of magnetic susceptibility. Paramagnetic behavior is observed above 7.1 K in $EuTe_4$ [162].

was observed that the critical temperature for superconductivity rises from 1.5 K to 3.5 K. The reason behind this was speculated to be either a structural phase transformation from orthorhombic to tetragonal phase or because of tellurium inclusions which themselves are superconducting above 5 GPa. It has also been observed that the magnetism in rare-earth tellurides is decoupled from the CDW and semiconducting states [257]. $T_{\rm CDW}$ of $GdTe_3$ also has a negative correlation with thickness (Fig. 10(e)) [161]. The reasons were attributed to the enhancement in the electron–phonon coupling, the chemical pressure on the $GdTe_3$ slab, and the expansion of the Te inner-layers. The ability to manipulate $T_{\rm CDW}$ by varying the thickness is useful as it may allow optical and electronic applications at RT.

Unlike other R-Te compounds, which show a metallic CDW, EuTe₄ has a semiconducting CDW. The reason being a nesting-

driven CDW phase lowering the electronic energy and imparting semiconducting properties. Hall measurements show that it is a p-type semiconductor with low carrier concentration. The magnetic susceptibility plots show $EuTe_4$ to have an antiferromagnetic phase transition with a Néel temperature, $T_N = 7.1$ K. A kink is observed in the temperature-dependence of electrical resistivity (Fig. 10(f)), indicating a first-order phase change [162].

Future perspectives

Interaction of Tellurium with various elements impart unique properties to the materials formed. Nanostructuring and obtaining 2D sheets further enhances these exciting properties. The review shows that while the 2D Te have the potential to bring significant advances to the technological field, a lot of work is required to improve our understanding of these tellurides, and

optimize them and their synthesis route to make full use of their properties. 2D tellurides show excellent superconductivity, electronic, and topological properties. The most important property is the versatility of tellurium and its ability to form compounds with such a large number of elements, despite having a weak chemical activity. The 2D structure provides dangling bonds for ion/molecule attachment which in turn provides better electrochemical performance. Some of the most advanced recent applications have been discussed in Supporting information [224,259–273].

Compared to tellurides of the type M_xTe_v , there are only a few experimental reports on ternary tellurides, with many reports being theoretical predictions. While electronic structure calculations can provide useful information about structural stability, optical and electronic behavior, it is still of fundamental importance to synthesize and characterize these materials in order to obtain a detailed understanding of their properties and test the feasibility of device fabrication. Various large scale synthesis like chemical vapour deposition methods and mechanical exfoliations are widely used [267,274]. Mechanical exfoliation, which started with scotch-tape to separate layers of graphene, has now improved where the adhesion of chemical bonds is used to obtain better morphology of the 2D materials. The deposition techniques like CVD and PVD have proven to be extremely useful in the synthesis of 2D materials, not just tellurides. Among all the synthesis methods, they have the highest yield and also gives precise control over the morphology, with desired large grain sizes, and orientation. Though we obtain a lesser yield, multilayer self-intercalation compounds can be synthesized by MBE methods for precise structure control [275,276]. MBE is a slow technique, but this works towards the advantage of researchers because it gives precise control over the grown layers, and allows monitoring the layers during their growth. Stable heterostructures can be fabricated with abrupt interfaces that are highly desirable in devices such as transistors. A disadvantage of MBE is that it has an extremely fast nucleation rate. This results in small grain sizes that may be undesirable for many applications. From the discussion on binary systems, we see that they behave very differently from sulfides and selenides, by exhibiting properties such as superconductivity, topological semimetallic properties, and supercapacitance. Doping or alloying them with another element can enhance their behaviour. For example, by alloying InTe with Fluorine, Rashba spin was brought forward in 2D InTeF. Adding a third element allows tuning the properties to obtain functionalized ternary tellurides [7].

Heterostructures are another venue that can be explored with 2D tellurides. Heterostructures provide flexibility in the bandgap values and can give us the ability to fine-tune the electronic and optical properties. It also helps to realize more functionalities with the 2D materials. A number of the above-mentioned materials, like ZnTe and $\rm In_2Te_3$, and $\rm InTeF$, have proven to perform well as heterostructures or show compatibility towards multiple materials. One easy way to obtain them is to let a layer of oxide formation on the surface. Oxide films have defects in them which act as additional states which enhance the optical properties of the material.

The optical properties of 2D tellurides are superior compared to their bulk parent materials. Their use will further enhance the optical behavior and broaden the optical range of absorption/emission when making optical hybrid/heterojunction devices. Their atomically-thin nature allows them to be deposited on existing optical devices to improve their performance. During the synthesis of 2D materials by mechanical exfoliation and other physical techniques, defects are introduced in the material. Defect engineering in 2D materials can improve the optical performance of devices. Large scale production and use of 2D tellurides in device applications are needed to make them competitive with their selenide and sulfide counterparts. Doping and alloying of 2D tellurides also remains largely unexplored.

A vast gap remains in our understanding of magnetic properties of 2D tellurides including the effect of layer thickness, substrate and the role of defects. The electrocatalytic activity of these 2D tellurides also needs more exploration. 2D tellurides provide several degrees of freedom to tune their catalytic properties. For instance, the exposed planes and active sites can be controlled using different synthesis technique. Alloying different cations can also improve the catalytic performance, as has been shown recently in 2D transition metal disulfides [7,277]. Catalysts are also greatly affected by external factors such as temperature, magnetic field and light exposure. 2D materials are highly surface sensitive, hence tuning the material based on the effects of these external factors can also open up new fields for research.

As discussed earlier in this Review, even though the topological properties of 2D tellurides have been studied theoretically, experimental verification of these predictions are still lacking. 2D structures of $\rm Bi_2Te_3$ are a prime example that have been predicted to be topological insulators but remain to be verified experimentally. Type-II Weyl semimetals also exhibit this nature. Further these materials can be chemically functionalized or doped to restrict the electron conduction to preferred channels in the material.

While 2D tellurides offer a lot of promise, the limited research which has existed for a long time restricts us from exploring all the possible applications of these materials. One of the reasons for this is the high toxicity of tellurium. There have been attempts to make thermoelectric generators to power biomedical devices [259]. Bi₂Te₃ was the material that was used in the studies, and the authors claim that in limited quantity, the material does not have adverse effects on the body. However, both bismuth and tellurides are toxic and in case of heavy exposures, can cause problems like skin rashes, diarrhoea, headache, drowsiness, nausea, tremors, and convulsions. Similar to bismuth telluride, CdTe also has applications in biological labels. However, studies carried out show that quantum dots of CdTe are not excreted out of the body through urine or stool and, due to its long half-life can have serious consequences to the body [278]. But given the therapeutic benefits of tellurium and its compounds, the means to modify the surfaces of the materials to make them more biocompatible needs to be devised.

Also, many of the known tellurides are unstable even in their bulk form, including some isolated 2D structures. They are highly prone to oxidation and defects are formed relatively easier. As tellurides are prone to oxidation, exposure of samples and devices to environmental is to be avoided by storing the sample in vacuum conditions. Fonseca et al. [58] have also reported that the properties of the synthesized sample do not

change when kept under vacuum conditions. In addition to chemical stability, ensuring structural stability is equally important. The 1T phase of VTe₂ is stable only in ML and for multilayer and bulk, the 1T structure distorts to form 1T' [279]. In some materials like ZnTe ML, strain is required to provide dynamic stability to the 2D layers. These challenges coupled with the satisfactory performance of the materials used commercially leads to the reluctance of adopting these materials for commercial applications. But even with limited research, the 2D telluride system has materials that show rich structural chemistry and unusual properties. The field holds a lot of promise and is certainly worth exploring. We hope the present work will contribute to further works on these exciting materials.

Conclusions

In this review, we have explored the most interesting properties of a wide array of emerging 2D tellurides. We start with a brief discussion of the structures and the properties of $M_x Te_y$ and $M_x N_y Te_z$, where M, N are elements other than Te and $x, y, z \ge 1$. Several of these materials are yet to be synthesized and their stability and properties have only been predicted by theoretical simulations. For the materials that have been synthesized, we have summarized the synthesis methods. Tellurides have been popular for their thermoelectric and topological properties, as the best known thermoelectric and Weyl semimetal are Bi_2Te_3 and WTe_2 respectively. In addition to these, we find there are also other properties such as superconductivity, magnetism (ferromagnetic, antiferromagnetic), supercapacitance, charge density waves, strain-tunable electronic and optical properties.

Declaration of Competing Interest

The authors declare that they have no known competing financial interests or personal relationships that could have appeared to influence the work reported in this paper.

Acknowldegement

P.K. and C.S.T. acknowledge AOARD (Asian Office of Aerospace Research and Development) grant no. FA2386-19-1-4039. C.S.T. acknowledges Ramanujan fellowship and core research grant of SERB, India. CST acknowledges the funding received from STARS project by MHRD, India. R.M. was supported through the National Science Foundation under grant number DMREF CBET-1729787.

Appendix A. Supplementary data

Supplementary data to this article can be found online at https://doi.org/10.1016/j.mattod.2021.08.008.

References

- [1] E. Lhuillier et al., Acc. Chem. Res. 48 (2015) 22–30.
- [2] S.-L. Li, Chem. Soc. Rev. 45 (2016) 118-151.
- [3] R. Li et al., Small. 14 (2018) 1802091.
- [4] K.S. Bhat et al., Electrochim. Acta 248 (2017) 188-196.
- [5] Y. Li et al., Adv. Energy Mater. 8 (2018) 1870106.
- [6] M. Asadi et al., ACS Nano. 10 (2016) 2167-2175.
- [7] Z. Hemmat et al., Adv. Mater. 32 (2020) 1907041.
- [8] L. Majidi et al., Adv. Mater. 31 (2019) 1804453.
- [9] Y. Zhang et al., Adv. Funct. Mater. 27 (2017) 1702317.
- [10] M. Popescu et al., J. Non-Cryst. Solids 352 (2006) 887–891.[11] K. Khan et al., J. Mater. Chem. C. 8 (2020) 387–440.

- [12] P. Kumbhakar et al., Mater. Today. 45 (2021) 142–168.
- [13] X. Jiang et al., Phys. Rep. 848 (2020) 1-58.
- [14] J. Pei et al., Adv. Mater. 31 (2019) 1706945.
- [15] M. Zhang et al., Adv. Opt. Mater. 7 (2019) 1800224.
- [16] M. Chhowalla et al., Nat. Chem. 5 (2013) 263–275.
- [17] J. Su et al., Adv. Mater. Interfaces 6 (2019) 1900741.
- [18] I. Terasaki et al., Compr. Semicond. Sci. Technol., Elsevier (2011) 326–358.
- [19] Z.-H. Ge et al., Scr. Mater. 143 (2018) 90–93.
- [20] J. Zhao et al., Inorg. Chem. 55 (2016) 3907-3914.
- [21] U.S. Shenoy et al., Chem. Phys. Lett. 651 (2016) 148-154.
- [22] N.D. Mermin et al., Phys. Rev. Lett. 17 (1966) 1133-1136.
- [23] C. Gong et al., Nature 546 (2017) 265-269.
- [24] Y. Ma et al., ACS Nano. 6 (2012) 1695-1701.
- [25] J.-U. Lee et al., Nano Lett. 16 (2016) 7433-7438.
- [26] L. Kang et al., Nat. Commun. 11 (2020) 3729.
- [27] M. Gibertini et al., Nat. Nanotechnol. 14 (2019) 408-419.
- [28] D.J. O'Hara et al., Nano Lett. 18 (2018) 3125-3131.
- [29] H. Hirai et al., J. Appl. Phys. 116 (2014) 083703.
- [30] J. Son et al., Nat. Commun. 7 (2016) 13261.
- [31] E.J.G. Santos et al., J. Phys. Chem. C 116 (2012) 7602–7606.
- [32] C. Lee et al., Science 321 (2008) 385–388.
- [33] J. Qiao et al., Nat. Commun. 5 (2014) 4475.
- [34] X. Wang et al., Nat. Nanotechnol. 10 (2015) 517-521.
- [35] F. Safari et al., Phys. E Low-Dimens. Syst. Nanostruct. 118 (2020) 113938.
- [36] Q. Wei et al., Appl. Phys. Lett. 104 (2014) 251915.
- [37] P. Huang et al., Nat. Commun. 11 (2020) 863.
- [38] G. Cassabois et al., Nat. Photonics 10 (2016) 262-266.
- [39] N.S. Eliseeva et al., JETP Lett. 95 (2012) 555-559.
- [40] W. Wang et al., 2D Mater. 8 (2021) 035058.
- [41] A. Jannat et al., Mater. Horiz. 7 (2020) 827-834.
- [42] G. Chen et al., Materials 13 (2020) 5515.
- [43] H. Zheng et al., Appl. Phys. Lett. 104 (2014) 132403.
- [44] S. Bertolazzi et al., ACS Nano. 5 (2011) 9703-9709.
- [45] K. Liu et al., Nano Lett. 14 (2014) 5097-5103.
- [46] D.A. Bandurin et al., Nat. Nanotechnol. 12 (2017) 223–227.
- [47] G.W. Mudd et al., Sci. Rep. 6 (2016) 39619.
- [48] J. Zhang et al., Nano Lett. 7 (2007) 2370-2376.
- [49] R. Roldán et al., J. Phys. Condens. Matter. 27 (2015) 313201.
- [50] V.-T. Pham et al., Sci. Rep. 10 (2020) 15082.
- [51] W. Chen et al., ACS Appl. Mater. Interfaces 10 (2018) 35289-35295.
- [52] F. Zhang et al., Adv. Electron. Mater. 6 (2020) 1900778.
- [53] W. Guo et al., Phys. Chem. Chem. Phys. 22 (2020) 4946-4956.
- [54] X. Zhang et al., Nanoscale 7 (2015) 16020-16025.
- [55] X.-H. Zha et al., Nanoscale 10 (2018) 8763–8771.
- $[56]\,$ A. Lipatov et al., Sci. Adv. 4 (2018) eaat 0491..
- [57] D.H. Keum et al., Nat. Phys. 11 (2015) 482-486.
- [58] J.J. Fonseca et al., Adv. Mater. 28 (2016) 6465–6470.
- [59] E. Vatansever et al., Mater. Res. Express. 5 (2018) 046108.
- [60] L. Guo et al. Nanoscale. 7 (2015) 11915-11921..
- [61] K.G. Wilson et al., Phys. Rep. 12 (1974) 75-199.
- [62] L. D. Landau et al., Butterworth-Heinemann, 1980..
- [63] P.W. Anderson, CRC Press, 2018..
- [64] C.L. Kane et al., Phys. Rev. Lett. 95 (2005) 146802.
- [65] C.-K. Chiu et al., Rev. Mod. Phys. 88 (2016) 035005.
- [66] X.-L. Qi et al., Rev. Mod. Phys. 83 (2011) 1057-1110.
- [67] W. Tian et al., Materials 10 (2017) 814.
- [68] H. Steiner et al., J. Appl. Crystallogr. 47 (2014) 1889-1900.
- [69] X.-B. Li et al., Phys. Rev. Lett. 116 (2016) 176803.
- [70] A.A. Burkov, Nat. Mater. 15 (2016) 1145–1148.
- [71] A.A. Soluyanov et al., Nature 527 (2015) 495–498.
- [72] I. Belopolski et al., Phys. Rev. B 94 (2016) 085127.
- [73] M. Yan et al., Nat. Commun. 8 (2017) 257.
- [74] P. Yu et al., Adv. Mater. 29 (2017) 1701909.
- [75] Y. Sun et al., Phys. Rev. B 92 (2015) 161107.
- [76] K. Deng et al., Nat. Phys. 12 (2016) 1105–1110.
- [77] S. Das et al., Annu. Rev. Mater. Res. 45 (2015) 1–27.
- [78] A. Laturia et al., Npj 2D Mater. Appl. 2 (2018) 1–7.
- [79] Y. Liu et al., Nat. Rev. Mater. 1 (2016) 1–17.
- [80] H. Yin et al., Chem. Soc. Rev. 45 (2016) 4873–4891.
- [81] S.B. Desai et al., Adv. Mater. 28 (2016) 4053-4058.
- [82] E. Gao et al., J. Mech. Phys. Solids 115 (2018) 248-262.
- [83] V. Nicolosi et al., Science 340 (2013).
- [84] J. Shen et al., Small 12 (2016) 2741-2749.

- [85] Q. Zhang et al., J. Mater. Chem. A 8 (2020) 15417-15444.
- [86] J. You et al., Nano Converg. 5 (2018) 26.
- [87] Q. Ji et al., Chem. Soc. Rev. 44 (2015) 2587-2602.
- [88] S.M. Rossnagel et al., J. Vac. Sci. Technol. A 21 (2003) S74–S87.
- [89] J.E. Greene et al., J. Vac. Sci. Technol. A 35 (2017) 05C204.
- [90] C. Muratore et al., Thin Solid Films 688 (2019) 137500.
- [91] B.A. Joyce et al., Rep. Prog. Phys. 48 (1985) 1637–1697.
- [92] L.A. Walsh et al., Appl. Mater. Today 9 (2017) 504-515.
- [93] M.B. Panish, Science 208 (1980) 916-922.
- [94] I. Khan et al., Nanotechnology 31 (2020) 195704.
- [95] B. Mortazavi et al., J. Mater. Chem. C 8 (2020) 2400-2410.
- [96] G.T. Lin et al., Phys. Rev. B 95 (2017) 245212.
- [97] C. Liu et al., Phys. Rev. Mater. 2 (2018) 094001.
- [98] B. Marfoua et al., ACS Appl. Mater. Interfaces 11 (2019) 38819–38827.
- [99] P. Chen et al., Nat. Commun. 8 (2017) 516.
- [100] X.-F. Tang et al., Phys. Rev. B 99 (2019) 125112.
- [101] B. Guster et al., 2D Mater. 6 (2018) 015027.
- [102] Y. Zhou et al., Phys. Rev. B 99 (2019) 125104.
- [103] S. Fragkos et al., Adv. Mater. Interfaces 6 (2019) 1801850.
- [104] H. Wang et al., ACS Nano. 13 (2019) 6008-6016.
- [105] P. Tsipas et al., ACS Nano. 12 (2018) 1696-1703.
- [106] X. Ma et al., ACS Appl. Mater. Interfaces 11 (2019) 10729-10735.
- [107] V. Musle et al., J. Alloys Compd. 770 (2019) 345-349.
- [108] T.-H. Lu et al., Chem. Commun. 51 (2015) 17012-17015.
- [109] X. Chia et al., Chem. Eur. J. 23 (2017) 11719-11726.
- [110] H. Ma et al., Chem. Mater. 30 (2018) 8891-8896.
- [111] T.A. Empante et al., ACS Nano. 11 (2017) 900-905.
- [112] J.-H. Huang et al., Adv. Mater. Interfaces 4 (2017) 1700157.
- [113] S. Yuan et al., Nat. Commun. 10 (2019) 1775.
- [114] C. Zhang et al., ACS Nano. 10 (2016) 7370-7375.
- [115] M. Li et al., Nanoscale 7 (2015) 15385–15391.
- [116] Y. Sharma et al., Opt. Mater. 33 (2011) 899-904.
- [117] P.K. Maheshwari et al., J. Supercond. Nov. Magn. 28 (2015) 2893–2897.
- [118] P.K. Maheshwari et al., J. Supercond. Nov. Magn. 31 (2018) 1659-1663.
- [119] T.-W. Hsieh et al., J. Phys. Condens. Matter. 30 (2018) 295303.
- [120] S. Liu et al., Npj 2D Mater. Appl. 1 (2017) 1-7.
- [121] H.-J. Deiseroth et al., Eur. J. Inorg. Chem. 2006 (2006) 1561–1567.
- [122] C. Tan et al., Nat. Commun. 9 (2018) 1554.
- [123] Z. Fei et al., Nat. Mater. 17 (2018) 778-782.
- [124] D. Kim et al., Nanotechnology 30 (2019) 245701.
- [125] H.L. Zhuang et al., Phys. Rev. B 93 (2016) 134407.
- [126] Z. Wang et al., Nano Lett. 18 (2018) 4303-4308.
- [127] X. Chen et al., Phys. Lett. A 379 (2015) 60-63.
- [128] Z. Zhang et al., Appl. Phys. Lett. 113 (2018) 142404.
- [129] X. Li et al., J. Mater. Chem. C 2 (2014) 7071.
- [130] S. Kang et al., J. Electron. Mater. 48 (2019) 1441-1445.
- [131] B. Marfoua et al., Phys. E Low-Dimens. Syst. Nanostruct. 126 (2021) 114443.
- [132] W. Zhou et al., Phys. Rev. Appl. 11 (2019) 064045.
- [133] W. Wang et al., Appl. Phys. Lett. 111 (2017) 203504.
- [134] C. Ke et al., J. Phys. Appl. Phys. 52 (2019) 115101.
- [135] J. Zhang et al., J. Mater. Chem. C 5 (2017) 8847-8853.
- [136] F.-B. Zheng et al., Phys. Chem. Chem. Phys. 22 (2020) 5163-5169.
- [137] Y. Zhu et al., Phys. E Low-Dimens. Syst. Nanostruct. 117 (2020) 113802.
- [138] K. Li et al., Appl. Surf. Sci. 471 (2019) 18–22.
- [139] Y. Saito et al., APL Mater. 6 (2018) 046104.
- [140] A. Mar et al., J. Am. Chem. Soc. 115 (1993) 3227-3238.
- [141] M. Zhao et al., ACS Nano. 13 (2019) 10705-10710.
- [142] T. Zhang et al., J. Phys. Chem. Lett. 11 (2020) 497-503.
- [143] Z. Zhu et al., Phys. Rev. Lett. 119 (2017) 106101.
- [144] T.T. Debela et al., J. Mater. Chem. C 6 (2018) 10218-10225.
- [145] P. Yu et al., Adv. Funct. Mater. 26 (2016) 137-145.
- [146] Y. Wang et al., Phys. E Low-Dimens. Syst. Nanostruct. 108 (2019) 53-59.
- [147] J. Li et al., Adv. Mater. 30 (2018) 1801043.
- [148] C. Battaglia et al., Phys. Rev. B 72 (2005) 195114.
- [149] C.W. Nicholson et al., Commun. Mater. 2 (2021) 1-8.
- [150] X. Yang et al., J. Mater. Chem. A 7 (2019) 27441-27449.
- [151] I. Sharma et al., Nanotechnology. 28 (2017) 445701.
- [152] Q. Zhao et al., Phys. Chem. Chem. Phys. 18 (2016) 18719-18726.
- [153] Y. Yu et al., Adv. Funct. Mater. 29 (2019) 1901012.
- [154] C. Han, Doctor of Philosophy Thesis, University of Wollongong, 2015.
- [155] S. Zhang et al., Sci. Rep. 9 (2019) 10951.
- [156] K. Chang et al., Science 353 (2016) 274-278.
- [157] Z. Fu et al., Phys. Rev. B 99 (2019) 205425.

- [158] F. Li et al., Adv. Mater. Interfaces 7 (2020) 2000410.
- [159] J.P. Heremans et al., Nat. Rev. Mater. 2 (2017) 1–21.
- [160] J. Lyu et al., ACS Appl. Mater. Interfaces 10 (2018) 43962-43969.
- [161] Y. Chen et al., Appl. Phys. Lett. 115 (2019) 151905.
- [162] D. Wu et al., Phys. Rev. Mater. 3 (2019) 024002.
- [163] Y. Deng et al., Nature 563 (2018) 94-99.
- [164] W. Gong et al., Appl. Phys. Lett. 114 (2019) 172104.
- [165] S. Nagata et al., J. Phys. Chem. Solids 54 (1993) 895-899.
- [166] H. Chen et al., Solid State Commun. 275 (2018) 16–20.
- [167] Y.-M. Chang et al., Adv. Mater. 30 (2018) 1706995.
- [168] K. Zhussupbekov et al., Npj 2D Mater. Appl. 5 (2021) 1–10.
- [169] X.-W. Tong et al., ACS Appl. Mater. Interfaces 12 (2020) 53921-53931.
- [170] E. Okogbue et al., Nanoscale. 12 (2020) 10647-10655.
- [171] T.-J. Ko et al., Appl. Mater. Today. 20 (2020) 100718.
- [172] G.J. Snyder et al., Nat. Mater. 7 (2008) 105-114.
- [173] R.J. Mehta et al., Nat. Mater. 11 (2012) 233-240.
- [174] R.J. Mehta et al., ACS Nano. 4 (2010) 5055-5060.
- [175] Y. Pei et al., Adv. Mater. 24 (2012) 6125-6135.
- [176] E. Ashalley et al., Front. Mater. Sci. 9 (2015) 103-125.
- [177] C. Nethravathi et al., J. Mater. Chem. A. 2 (2013) 985-990.
- [178] Y. Pang et al., Phys. Rev. Mater. 4 (2020) 094205.
- [179] S. Zhou et al., Npj Quantum Mater. 3 (2018) 16.
- [180] H.L. Zhuang et al., Chem. Mater. 25 (2013) 3232-3238.
- [181] B. Wu et al., Sci. China Mater. 60 (2017) 747-754. [182] M. Naseri et al., Chem. Phys. Lett. 707 (2018) 160-164.
- [183] R. Chaurasiya et al., J. Appl. Phys. 125 (2019) 082540. [184] S.I. Kim et al., Science 348 (2015) 109-114.
- [185] S.H. Zaferani et al., Adv. Eng. Mater. 23 (2021) 2000816.
- [186] P. Guo et al., J. Phys. Condens. Matter. 32 (2020) 325502.
- [187] Q. Wang et al., Nano Lett. 19 (2019) 2647-2652.
- [188] P. Hu et al., Nano Lett. 13 (2013) 1649-1654.
- [189] F. Liu et al., ACS Nano. 8 (2014) 752-760.
- [190] S. Huang et al., ACS Nano. 10 (2016) 8964-8972.
- [191] P. Hu et al., Nano Res. 7 (2014) 694-703.
- [192] S. Siddique, A.C.S. Appl, et al., Nano Mater. (2021).
- [193] N. Fatahi et al., Eur. Phys. J. B 93 (2020) 32.
- [194] A.M. Gabovich et al., Adv. Condens. Matter Phys. 2010 (2010) 1-40.
- [195] B. Guo et al., Laser Photonics Rev. 13 (2019) 1800327.
- [196] R. Wu et al., Nano Lett. 11 (2011) 5159-5164.
- [197] F. Bonaccorso et al., Nat. Photonics 4 (2010) 611-622.
- [198] J. Zhang et al., Opt. Lett. 41 (2016) 1704-1707.
- [199] L. Wu et al., Adv. Funct. Mater. 29 (2019) 1806346.
- [200] J. Lee et al., Sci. Rep. 10 (2020) 15305.
- [201] J. Susoma et al., Appl. Phys. Lett. 108 (2016) 073103.
- [202] B. Lei et al., Chin. Phys. B 29 (2020) 058104. [203] M. Wang et al., ACS Appl. Mater. Interfaces (2020).
- [204] S.S. Abed Al-Abbas et al., Superlattices Microstruct. 135 (2019) 106245.
- [205] A. Kudo et al., Chem Soc Rev. 38 (2009) 253-278.
- [206] B. Ye et al., RSC Adv. 8 (2018) 7997-8006.
- [207] T. Gorkan et al., J. Phys. Chem. C 124 (2020) 12816-12823.
- [208] M.-W. Lin et al., J. Mater. Chem. C. 4 (2015) 315-322.
- [209] L.D. Casto et al., APL Mater. 3 (2015) 041515.
- [210] C. Song et al., Phys. Rev. B 99 (2019) 214435.
- [211] S. Albarakati et al., Sci. Adv. 5 (2019) eaaw0409..
- [212] A.F. May et al., ACS Nano. 13 (2019) 4436-4442.
- [213] M. Joe et al., Nano Mater. Sci. 1 (2019) 299-303.
- [214] T. Ohta et al., AIP Adv. 11 (2021) 025014. [215] M.N. Ali et al., Nature 514 (2014) 205-208.
- [216] J. Augustin et al., Phys. Rev. B 62 (2000) 10812-10823.
- [217] P. Li et al., Nat. Commun. 8 (2017) 2150.
- [218] H.B. Nielsen et al., Phys. Lett. B. 130 (1983) 389-396.
- [219] Y.-Y. Lv et al., Phys. Rev. Lett. 118 (2017) 096603.
- [220] F.-X. Xiang et al., Phys. Rev. B 98 (2018) 035115. [221] X. Shen et al., Appl. Phys. Lett. 109 (2016) 113104.
- [222] R. Bhattarai et al., Appl. Phys. Lett. 116 (2020) 023101.
- [223] H. Guo et al., Superlattices Microstruct. 137 (2020) 106326. [224] Y. Bao et al., J. Phys. Appl. Phys. 52 (2018) 075103.
- [225] L. Fu et al., Phys. Rev. Lett. 98 (2007) 106803.
- [226] Y.-Y. Li et al., Adv. Mater. 22 (2010) 4002–4007.
- [227] D. Hsieh et al., Nature 460 (2009) 1101-1105. [228] C.-X. Liu et al., Phys. Rev. B 81 (2010) 041307.
- [229] C. Wang et al., Phys. Rev. B 94 (2016) 241119.
- [230] Y. Wu et al., Phys. Rev. B 94 (2016) 121113.

- [231] S. Tang et al., Nat. Phys. 13 (2017) 683-687.
- [232] S. Wu et al., Science 359 (2018) 76-79.
- [233] F. Lüpke et al., Nat. Phys. 16 (2020) 526-530.
- [234] F. Zheng et al., Adv. Mater. 28 (2016) 4845-4851.
- [235] Z. Fei et al., Nat. Phys. 13 (2017) 677-682.
- [236] M. Yoshida et al., Nano Lett. 18 (2018) 3113-3117.
- [237] R. Zhou et al., Crystals. 10 (2020) 575.
- [238] E. Haubold et al., Phys. Rev. B 95 (2017) 241108.
- [239] Y. Deng et al., Science 367 (2020) 895-900.
- [240] H. Li et al., Phys. Chem. Chem. Phys. 22 (2020) 556-563.
- [241] J. Zhou et al., Adv. Sci. 8 (2021) 2003832.
- [242] M.J. Shu et al., Appl. Phys. Lett. 104 (2014) 251907.
- [243] M. Wuttig et al., Nat. Mater. 6 (2007) 824-832.
- [244] Y. Li et al., Nat. Commun. 7 (2016) 10671.
- [245] Y. Wang et al., Nature 550 (2017) 487-491.
- [246] F. Zhang et al., Nat. Mater. 18 (2019) 55-61.
- [247] S. Song et al., Nano Lett. 16 (2016) 188-193.
- [248] W. Hou et al., Nat. Nanotechnol. 14 (2019) 668-673.
- [249] S. Cho et al., Science 349 (2015) 625-628.
- [250] P. Yu et al., Adv. Mater. 29 (2017) 1603991.
- [251] H.P.D. Lanyon et al., J. Appl. Phys. 35 (2004) 1516.
- [252] A. Bhargava et al., J. Non-Cryst. Solids 192-193 (1995) 494-497.
- [253] A. Manchon et al., Nat. Mater. 14 (2015) 871-882.
- [254] Y. Ma et al., Phys. Chem. Chem. Phys. 16 (2014) 17603.
- [255] A. Perucchi et al., Eur. Phys. J. B 48 (2005) 489-493.

- [256] M. Hoesch et al., Phys. Rev. B 93 (2016) 125102.
- [257] D.A. Zocco et al., Phys. Rev. B 91 (2015) 205114.
- [258] Q. Li et al., Nano Lett. 18 (2018) 7962-7968.
- [259] M. Koplow et al., 5th Int Summer Sch. Symp. Med. Devices Biosens. 2008 (2008) 322–325.
- [260] Y.-F. Lin et al., Adv. Mater. 26 (2014) 3263-3269.
- [261] N.R. Pradhan et al., ACS Nano. 8 (2014) 5911-5920.
- [262] J. Tian et al., Sci. Adv. 3 (2017) e1602531.
- [263] J.-L. Xu et al., Sci. Rep. 5 (2015) 14856.
- [264] D. Pesin et al., Nat. Mater. 11 (2012) 409-416.
- [265] Y. Ando et al., Nano Lett. 14 (2014) 6226-6230.
- [266] D. Won et al., Adv. Mater. 32 (2020) 1906578.
- [267] X. Xu et al., Science 372 (2021) 195-200.
- [268] Z. Shi et al., Nano-Micro Lett. 12 (2020) 99.
- [269] H. Wang et al., Chem. Res. Chin. Univ. 36 (2020) 551–559.
- [270] L. Tao et al., J. Am. Chem. Soc. 140 (2018) 8696–8704.
- [271] J.P. Fraser et al., ACS Appl. Mater. Interfaces 12 (2020) 47774–47783.
- [272] L.M. Nieves et al., Nanoscale 13 (2021) 163-174.
- [273] M.-A. Shahbazi et al., Chem. Soc. Rev. 49 (2020) 1253-1321.
- [274] Y. Guo et al., ChemNanoMat. 7 (2021) 323-327.
- [275] K. Lasek et al., ACS Nano. 14 (2020) 8473-8484.
- [276] P.K.J. Wong et al., ACS Nano. 13 (2019) 12894-12900.
- [277] J. Cavin et al., Adv. Mater. (2021) 2100347.
- [278] Y.-F. Li et al., Small 7 (2011) 2965-2980.
- [279] P.M. Coelho et al., J. Phys. Chem. Lett. 10 (2019) 4987–4993.